arXiv:1409.6174v1 [astro-ph.GA] 19 Sep 2014

Probing Accretion Disk Winds in AGN

I. Asymmetric broad Balmer emission lines

Cosmos DUMBA
Department of Physics, Faculty of Science
Mbarara University of Science & Technology
P. O. Box 1410, Mbarara, Uganda

September 23, 2014

The Broad Line Region of Active Galactic Nuclei is characterized by broad Balmer emission lines in their optical spectra. The broad Balmer emission lines are found to be asymmetric, some blue sided and others red sided in their asymmetry. One of the components behind the asymmetry is thought to be an accretion disk wind. We probe the accretion disk wind using the broad balmer emission line profiles.

This asymmetry of the broad balma emission line profiles is measured in velocity space after a measurement of the line shift at percentiles from 0, in increaments of 10, up to 90. In addition, the Kurtosis Index is obtained at appropriate points of the emission lines' profiles. This study is based on many hundreds of SDSS spectra, starting with low redshift high signal to noise ratio spectra. We also consider a definite number in each bin of their FWHM, in bins of 1000 km/s (atleast 40 per bin), starting from 1000km/s to the very broad emission lines.

We present how strong the asymmetry (by plotting Asymmetry Index as a function of percentile) of the broad/narrow lines (in percent) is, what the Kurtosis $(R20, 80)$ is. We also present what the Asymmetry Index as a function of line width (FWHM), luminosity (V-band), core-radio flux and Ionization Degree.

AGN: Accretion Disk, Accretion Disk Wind – Line: Asymmetry, Balmer, Emission, Profiles

1 Introduction

Active Galaxies have been widely studied by many authors revealing many fascinating properties which among all include; compact nuclear emission (Clavel et al. 1990), non-thermal continuum emission

$$F_\nu \sim \nu^{-\alpha} \tag{1}$$

(Bregman 1990).
In addition, authors notice that; the continuum stretches from the radio to X-ray/Gamma rays (Mehdipour et al. 2011), the luminosity of the nucleus exceeds that of the host (Osterbrock 1989), they have strong emission lines (De Breuck et al. 2000), are highly variable (Ulrich et al. 1997), and also have X-ray emission (Turner & Pounds 1989).
The energy source in the AGN is believed to be accretion (Blandford & Znajek 1977). This can be demonstrated through the relation :

$$E = \eta m c^2 \tag{2}$$

where η is the efficiency.
The luminosity can then be re-written as:

$$L = \frac{dE}{dt} = \eta \frac{dM}{dt} c^2 = \eta \dot{M} c^2 \tag{3}$$

where $\dot{M} = \frac{dM}{dt}$ is the accretion rate.
For a typical AGN;

$$\dot{M} = \frac{L}{\eta c^2} \approx 1.8 \times 10^{-3} \frac{L_{37}}{\eta} M_{sun} yr^{-1} \tag{4}$$

where L_{37} is the luminosity in units of 10^{37} W.
This energy, at one point, through the principle of hydrostatic equilibrium, reaches a point at which gravitational forces (causing the accretion) balance with radiative forces (from the nucleus). This limit defines a characteristic luminosity, the Eddington luminosity (L_{Edd}) through the relations;

$$F_{grav} = F_{rad} \tag{5}$$

$$\frac{GM(m_p + m_e)}{r^2} \approx \frac{GMm_p}{r^2} = \frac{\sigma_T L_{Edd}}{4\pi c r^2} \tag{6}$$

$$L_{Edd} = \frac{4\pi G m_p c}{\sigma_T} M \tag{7}$$

$$L_{Edd} = 1.26 \times 10^{31} \frac{M}{M_{sun}} [W] \tag{8}$$

The important parameter in AGN is $\frac{L}{L_{Edd}}$.
One of the consequences of high $\frac{L}{L_{Edd}}$ are winds, Accretion Disk Winds. Just like in Solar Winds....once a particle exceeds the escape velocity, we see this as a wind from the accretion disk. Accretion disk winds have been confirmed by some authors by studying BAL Quasars (Hamann 1998). Hamann (1998) observed strong absorption troughs in the rest-frame UV spectrum and estimated outflows with 10,000 km/s.

In this work, we study the accretion disk

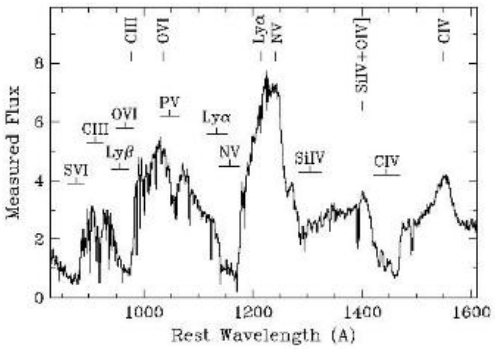


Figure 1: The rest frame of the UV spectrum of a BAL Quasar showing a significant outflow in the absorption lines of up to 10,000 km/s
Hamann (1998)

winds by analysing broad Balmer line profile

asymmetry and steepness values.
We define the two parameters in line shape analysis as:

$$A.I = \frac{S}{IPV} \tag{9}$$

$$K.I = \frac{IPV_U}{IPV_L} \tag{10}$$

where S is the line shift, IPV is the interpercentile velocity, IPV_U and IPV_L are the interpercentile velocities for the upper and lower parts of the emission line profile. The following sections will outline what we did in more detail and explain the most important steps we carried out during the study.

2 Data

2.1 Introduction to Data Analysis

In order to study any sample of galaxies and quasars, it is important not to forget a few useful conditions that make the sample produce reliable information:

- the size of the sample and
- the quality of the spectra, both in terms of resolution and Signal to Noise ratio.(Whittle 1985a)

Our data meets both criteria thanks to dedicated surveys like the SDSS that have made such homogeneous data sets available to the public.
We have obtained, in each sample, the top 600 high signal to noise galaxies and quasars from the seventh data release (DR7) (York et al. 2000). The samples have the highest spectroscopic quality in the release (Abazajian et al. 2009), and are uniform in terms of calibration let alone being complete.
We have two samples for the same reasons of obtaining quality spectra in all ranges of FWHM from 1000 km/s to above 10,000 Km/s. This is so because as we are selecting the spectra with the highest signal to noise ratio, there is a tendency to obtain only spectra that are both from sources near (low redshift), thus neglecting those with higher redshift, and also biasing the data primarily on signal to noise ratio. This is avoided when we split the sample in two samples, one for those between 1000 km/s FWHM and 3000 km/s FWHM, and another for those having FWHM greater than 3000 km/s. We end up having spectra with very high signal to noise ratio across the whole spectrum of broad Balmer emission lines. Remember broad Balmer emission lines are those with FWHM greater than 1000 km/s.
In this section, we explain how we download the data, how we treat the data, describing the software we use and all the tasks used. We also explain all the steps we carry out, giving details of the output in each step and why it is carried out. In addition we show samples of the values extracted from the plots (the whole list being found in the appendices). Lastly we describe the secondary treatment of the extracted data from the plots, explaining how and why we carried out the treatment in such ways and show samples of the results in tables (the actual results being shown in the next chapter). But then, it is necessary to first briefly describe the database (SDSS) and thereafter the telescope and the surveys it has carried out so that one gets a feeling of the whole process from observing, collection of data, treatment of data and analysis.

2.1.1 SDSS Database

The Sloan Digital Sky Survey consists of three major surveys that together provide scientists with immense volumes of data obtained from a dedicated 2.5m telescope lo-

cated at Apache Point Observatory in Southern New Mexico. This survey has been collecting data since the year 2000 (Abazajian et al. 2009; York et al. 2000). The three surveys are;

- Legacy
- SEGUE
- Supernova

2.1.2 SDSS Legacy Survey

The SDSS Legacy Survey provided a uniform, well-calibrated map in ugriz of more than 7,500 square degrees of the North Galactic Cap, and three stripes in the South Galactic Cap totaling 740 square degrees. The central stripe in the South Galactic Gap, Stripe 82, was scanned multiple times to enable a deep co-addition of the data and to enable discovery of variable objects. Legacy data supported studies ranging from asteroids and nearby stars to the large-scale structure of the universe. Almost all of these data were obtained in SDSS-I, but a small part of the footprint was finished in SDSS-II.

2.1.3 SEGUE - Sloan Extension for Galactic Understanding and Exploration

SEGUE was designed to explore the structure; formation history; kinematics; dynamical evolution; chemical evolution; dark matter distribution of the Milky Way. The images and spectra obtained by SEGUE allowed astronomers to map the positions and velocities of hundreds of thousands of stars, from faint, relatively near-by (within about 100 parsec or roughly 300 light-years) ancient stellar embers known as white dwarfs to bright stellar giants located in the outer reaches of the stellar halo, more than 100,000 light-years away. Encoded within the spectral data are the composition and temperature of these stars, vital clues for determining the age and origin of different populations of stars within the Galaxy (Yann et al. 2009).

2.1.4 The SDSS Supernova Survey

The SDSS Supernova Survey was one of three components (along with the Legacy and SEGUE surveys) of SDSS-II, a 3-year extension of the original SDSS that operated from July 2005 to July 2008. The Supernova Survey was a time-domain survey, involving repeat imaging of the same region of sky every other night, weather permitting. The primary scientific motivation was to detect and measure light curves for several hundred supernovae through repeat scans of the SDSS Southern equatorial stripe 82 (about 2.5° wide by 120° long) (Frieman et al. 2008). The above three surveys have provided scientists with a catalog derived from the images obtained by the 2.5m telescope. These images include more than 350 million celestial objects, and spectra of 930,000 galaxies, 120,000 quasars, and 460,000 stars. This data is not only fully calibrated and reduced, carefully checked for quality, and publicly accessible through efficient databases, but has also been been publicly released in a series of annual data releases. It is through this effort that we are able to carry out this study on the asymmetry of the broad emission lines of active galactic nuclei.
In this Data release, this study exploits the immense volume of spectra of galaxies and quasars (Abazajian et al. 2009; York et al. 2000). The sample obtained from the release includes around 600 spectra of both galaxies and quasars in the redshift range of 0 and 1, with broad Hβ lines from 1500km/s enabling us contain all groups of broad line emission objects.SDSS (2013)



Figure 2: The 2.5m telescope located at Apache Point Observatory in Southern New Mexico BBC (2013)

2.1.5 Obtaining the Data

In order to obtain data from the SDSS database with your own constraints on the sample, one needs to write an SQL Query that generates a list of the sources that meets your requests.

In this study, we focus on the parameters of the $H\alpha$ & Hβ emission line, looking for asymmetry in these lines.

2.1.6 Data Properties and Constraints Invoked

The data in our samples combined consists of around 300 objects, galaxies and quasars, restricted to a redshift range between 0 and 1. The samples consist of reduced spectra of these objects in fits files that we renamed in ascending order from those with the highest signal to noise ratio. This helps us analyze those with the highest signal to noise ratio first. This is important because the results obtained from high signal to noise ratio sources are more reliable for the derivation empirical relations. The redshift limit was chosen so that we have a good coverage of the Hβ line and its adjacent spectral regions. Figure presents the general properties of the sample in terms of redshift, signal to noise ratio and the broadening of the Hβline.

In addition, this data consists of around 283 spectra with measured $H\beta$ profiles around 165 measured $H\alpha$ profiles. This is because not all spectra could have both the $H\beta$ emission line and $H\alpha$ emission line due to redshifting at both ends of the optical window. However, most of the spectra with $H\beta$ lines also have $H\alpha$ lines but not vice versa. Of course spectra that are at the extreme end of our redshift selection are the ones affected with not having the $H\alpha$ line visible, but this is not an issue for us to worry about since we were more interested in the $H\beta$ line profiles.

Figures 3 show the distribution of the signal to noise ratio of our sample and the redshift. It is seen here in the signal to noise distribution that we have a fairly good signal to noise ratio, the minimum being 37 and maximum 79. The distribution is binned in 5 starting from 35. The figure therefore clearly shows that most of our sample spectra have a signal to noise ratio between 40 and 45, to be specific around 120 out of 300 (40%), with a few having more than that. This is not a problem since, given the nature of our study, a signal to noise ratio of even 30 would be sufficient for good measurements (Thorne et al. 1999).

In the same way, the redshift distribution is shown. Because we chose spectra with the

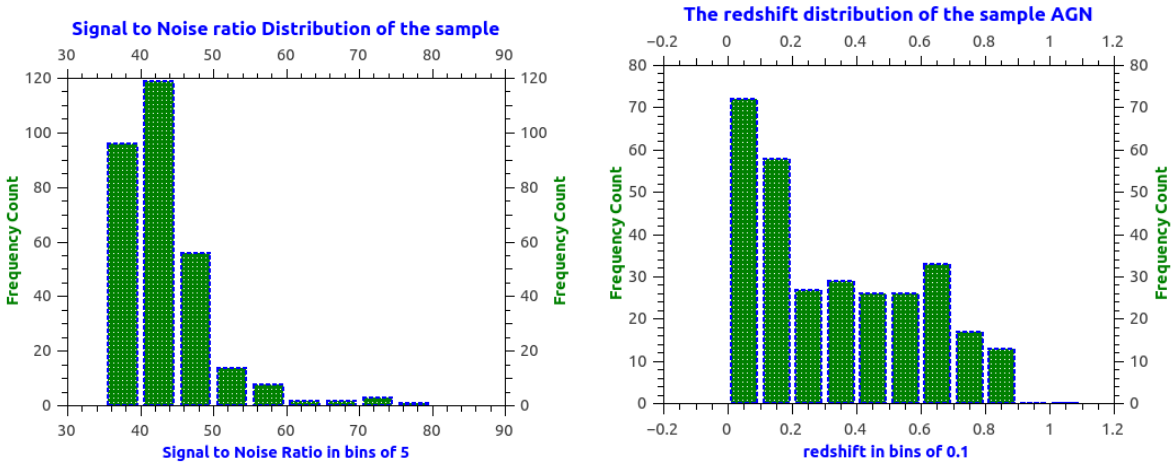


Figure 3: Signal to Noise ratio & Redshift distribution of Sample

highest signal to noise ratio, it seemed obvious that most of the sample spectra will be in the near end of the redshift window we chose with those below redshift 0.2 dominating. However, since the distribution does not fall rapidly as we move to higher redshift, the data will provide a sufficient study of AGN within this redshift bin chosen. In a later study, it would be good to also study other redshift ranges, possibly using Ultraviolet emission lines which can be obtained in the optical spectra after they have been red shifted.

Figures 4 show the distribution of the FWHM of all the $H\beta$ emission lines measured. The distribution shows that there is a peak between 3000 km/s and 4000 km/s. But still it is not a big range from the bins at both ends which are at 50 each. Our intention is to have a good distribution across the whole range from 1000 km/s to over 10,000 km/s, and since we obtain enough counts for the first five bins, then the sample will provide a statistically sufficient analysis for our findings.

The other figure here is a cumulative distribution, which shows that from FWHM of 9000 km/s, there isn't any increase in counts as there are very few AGN with such extremely broad lines. Our study will obtain information about the broad lines basing almost entirely on the first six or seven bins with sufficient numbers.

The distribution of the FWHM in our sample is in agreement with the AGN statistics obtained by Hao et al. (2005) when they plotted the distribution of the FWHM values of the $H\alpha$ emission line for over 40,000 emission line galaxies. Their distribution was bimodal since they included all AGN, narrow and broad line AGN. Their boarder line of broad line AGN was naturally placed at those with a FWHM of over 1200 km/s. To compare with our distribution, we only consider those over 1000 km/s, and it gives us the same distribution. In their study, defining broad line AGN as objects with a FWHM greater than 1200 km/s, they obtained 1,317 objects out of 42,435 emission line galaxies. This makes our sample of 300 objects not bad since it is a quarter of this value, let alone having been restricted to a redshift between 0 and 1.

Following this simple look at the general properties of the downloaded data, it is

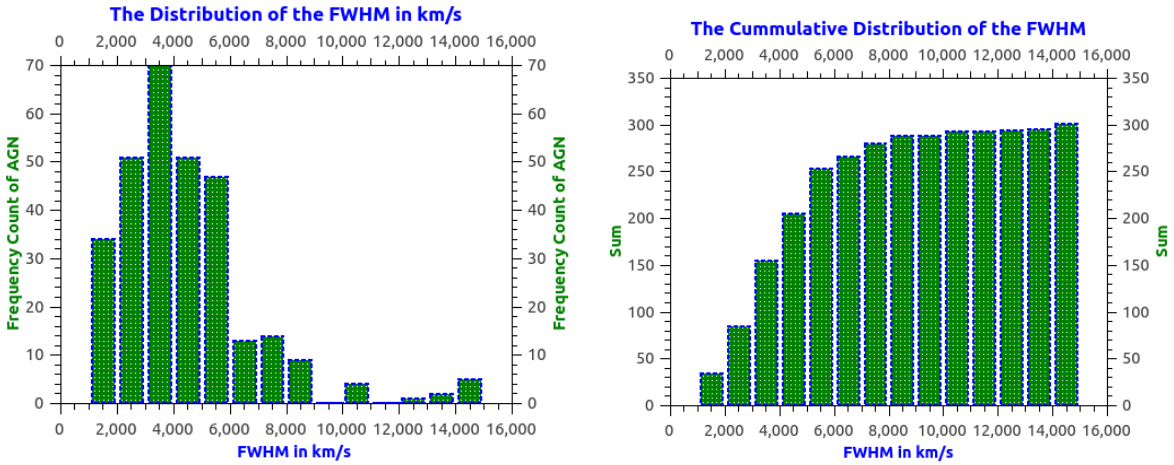


Figure 4: Full Width at Half Maximum distribution of Sample

now necessary to explain the treatment of the data in order to obtain measurements that are needed for our later analysis. The detailed spectral properties of the sample will follow later in the forthcoming chapters.

2.2 Image Plotting and Analysis with IRAF

IRAF (an acronym for Image Reduction and Analysis Facility) is a collection of software written at the National Optical Astronomy Observatory (NOAO) geared towards the reduction of astronomical images in pixel array form. In this thesis, i used IRAF to plot spectra from our sample AGN and analyzed a few spectral lines needed to derive more information for analysis later (Tody 1986; Valdes 1986). To be specific, we plotted the Balmer lines, $H\alpha$ and $H\beta$ emission lines, although not all spectra contained both emission lines. Most of them had the $H\beta$ emission line, a good number had both $H\beta$ and $H\alpha$ emission line, while very few($\sim$2%) had only the $H\alpha$ emission line.

In the following subsections, i will explain briefly the steps and tasks i used to extract the information i needed from the broad Balmer lines in my sample. This was principally the part of the thesis that occupied me most since it involved careful visual analysis of the spectrum first and accurate execution of the required commands for which a mistake with one of them means redoing the whole process from the beginning. Explained below are the steps i took during my data extraction.

2.2.1 Spectrum Visual Analysis

After downloading the data, (the fits files), and having renamed them, starting from the one having the highest signal to noise ratio, i plotted each spectrum and analyzed the Balmer emission lines. The reason why i needed to do this is because each spectrum is unique and the tasks to perform on each varied from one spectrum to another. Some of the things i looked out for were;

- The availability of both $H\beta$ and $H\alpha$ emission lines.
- Iron emission around the $H\beta$ emission line, the Fe Emission.
 This was important to note because a lot

of Fe emission could provide a poor estimate for the continuum measurements. If the emission was only on either side of the Balmer line, i would use the end with less emission as my proxy for the continuum. In cases where there was too much Fe emission, i excluded such a spectrum from my sample since it meant an extra process of using a template to subtract the Fe emission first.

- Availability of neighboring narrow lines ([OIII] for $H\beta$ & [SII] for $H\alpha$).
 This was for use in estimating an equivalent FWHM of the narrow component to subtract from the Balmer line. However, for the case of the $H\alpha$ emission line, the [SII] emission doublet was not accurate enough because the two lines were blended together in most cases. It meant using the [NII] lines that were within the broadened $H\alpha$ emission. This meant a visual estimation once both [SII] & [NII] lines were unavailable. On a positive note, there were very few cases where i could not use any of the two.

- The function to use while subtracting the continuum.
 This was important because the uniqueness of each spectrum, and the quest to apply a good estimate to a flat spectrum, entails using different functions for each spectrum in order to obtain a flat spectrum from the power law spectra downloaded.

All the above mentioned reasons vary from spectrum to spectrum and each of them is important in order for me to obtain the best results from the spectrum, and for minimizing errors as much as i can.
In our data, which has two samples, sample 1 being that of AGN with FWHM between 1000 km/s and 3000 km/s, and sample 2 being that of AGN with FWHM from 3000 km/s and above, this is what we observed from the visual analysis;

- The AGN in sample 1 have both $H\alpha$ and $H\beta$, meaning they are found in the lower part of the redshift range from 0 to 1, preferably less than z = 0.6. There are less than 10 out of 81 that had only the $H\beta$ emission line.

- Sample 2 has at least 40% of the AGN having both $H\alpha$ and $H\beta$. This means 60% of them are found in the higher end of the redshift bin, preferably above z = 0.7. Recall that my redshift range is from z = 0 to z = 1.

2.2.2 Continuum Subtraction

This is the task done after visual analysis of the spectrum. Spectra with both the $H\alpha$ and $H\beta$ emission lines look similar to the ones in figure 5 although some with significant redshift will only have the $H\beta$ emission line still available. The subtraction of the continuum is done in splot, with the keys "t" followed by a "-", followed with the appropriate function necessary for the selected region. The continuum is subtracted for each emission line separately and separate images are saved out of the original image having both emission lines. This can be seen in the sample plots in figure 6 on page 9. Continuum subtraction is the second step to spectrum analysis for the Balmer emission line features and it sets a vantage point for line normalization, as we shall discuss in the next subsection.

2.2.3 Line Normalization

To normalize the emission line simply means to have its base at a zero point and its peak

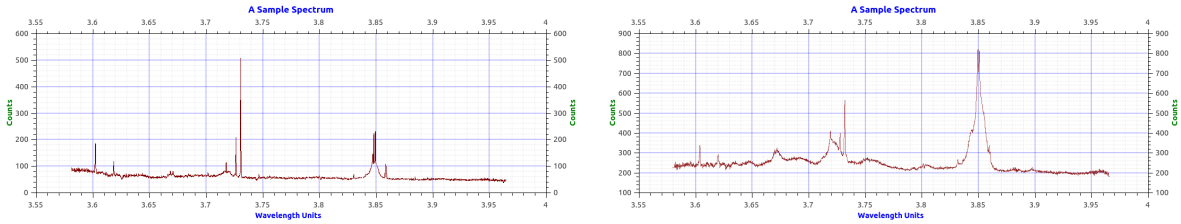


Figure 5: Seen above are two samples of the spectra during visual analysis. It should be noted that not all spectra contain the $H\alpha$ and $H\beta$ emission lines as seen here, reason being that those red-shifted significantly will eliminate the $H\alpha$ since it will be Doppler shifted to wavelengths outside the optical range. In addition, not all spectra are relatively flat like the ones shown due to the varying amounts of continuum emission at different wavelengths for many AGN

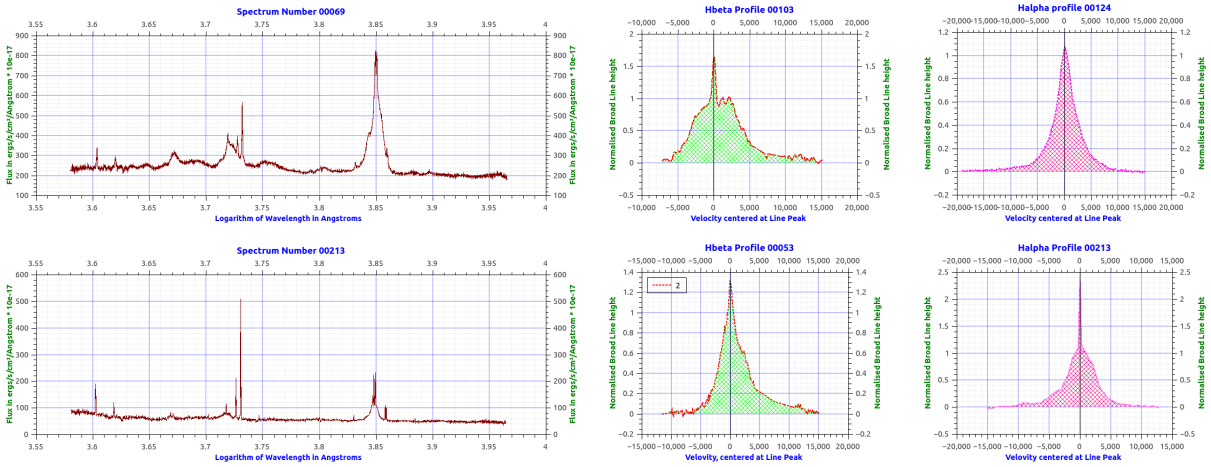


Figure 6: The images show an example of extracted Balmer emission lines after continuum subtraction on each of them. One should note here that all the extracted emission lines have their continuum at zero, making it the starting point of the percentile ranges we need examine later.

at unity. It should be noted that we are normalizing the broad Balmer lines. This means that we either subtract the narrow components or simply leave them visible, but ignore their additional height as we simply place a unity value at the peak of the broad line.

In the figure 7, examples on the diversity of broad and narrow components in our sample with some not having narrow components at all and others dominated by the narrow component are shown.

To perform the normalization of the broad Balmer emission lines, we use the arithmetic task, "imarith", which can be used anytime in IRAF. However, after continuum subtraction, the counts at the peak of the broad Balmer line are recorded in a table. Also in the same table is recorded the velocity at which the emission line is centered. This velocity will be of use while transforming to velocity space, centering the emission line peak at that velocity.

Table 1 shows part of the table. The whole table can be viewed in the appendices section. It shows the Spectrum Number, the Balmer line heights used to normalize the profile to unity and the corresponding wavelengths at which they are identified. These wavelengths are the wavelengths at which we center the corresponding lines while transforming to velocity space.

2.2.4 Line Correction : Filtering out other lines and Smoothening out the noise

In any spectrum, there is always a probability that the emission line you are interested in is surrounded by other emission or absorption lines. For some emission lines, the neighboring emission lines or absorption lines are not a threat to any measurements pertaining the emission line under study, for example, for the $H\alpha$ emission line, the neighboring Sulphur II emission lines do not pose a threat to any measurements needed from the $H\alpha$ emission line. This can be seen in the examples below.

However, for the $H\beta$ emission line, there is an undeniable problem. The neighboring emission lines are significant enough to pose a threat to measurements taken from it. These emission lines are; the Oxygen III lines and the Iron emission at both sides of the $H\beta$ emission line. The Iron emission will increase on the error in the continuum subtraction since it creates a pseudo continuum and thus making it difficult to estimate a continuum level. To reduce on the error in this measurement, one has to subtract the iron emission, preferably using some already developed templates before the actual continuum level can be estimated.
In our case, since it was a small fraction of spectra that had significant iron emission on both sides, we neglected this since it affects less than 5% of the data. The Oxygen III emission lines also increase on the uncertainty of the FWHM values measured since they are embedded in the broad Balmer $H\beta$ emission lines. The most reliable way to deal with this uncertainty is to subtract them before any values are measured. However, since they are also broadened at their bases, their subtraction, using a Gaussian model, increases absorption features in the residue $H\beta$ emission line left. Thus, since the emission lines are already broad, we decided to simply cut them out in order to leave a smoother profile for the residue for better measurements without introducing a smoothing factor. It is noticed that subtracting the OIII lines introduces absorption features which in turn adds an uncertainty to the measurements, so simply cutting them off and preventing this uncertainty seemed better because the uncertainty we deal with by not doing the subtraction itself is much less.

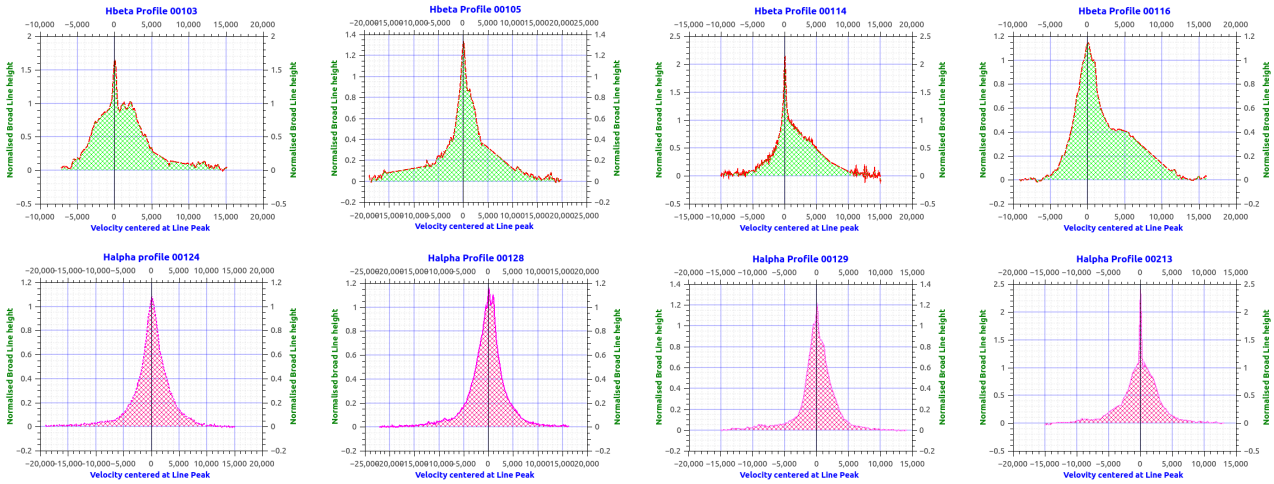


Figure 7: The images show an example of the normalized broad Balmer emission lines after continuum subtraction on each of them. It is clear from these examples, the diversity of broad and narrow components in AGN permitted emission lines

Table 1: A table showing the initial values extracted from each spectrum plot for Line Normalization and Velocity Transformation.

Spectrum Number	Hα height	Centering λ(Å)	Hβ height	Centering λ
00001(ha & hb.fit)			88.01	7353.861
00002(ha & hb.fit)			58.36	8599.299
00003(ha & hb.fit)			39.25	7235.383
00004(ha & hb.fit)	354.4	7365.362	87.10	5455.679
00005(ha & hb.fit)	258.2	8927.240	88.46	6612.635
00006(ha & hb.fit)	414.5	6785.756	140.0	5026.721
00007(ha & hb.fit)			22.12	6819.172
00008(ha & hb.fit)	173.7	6837.628	44.66	5064.256
00009(ha & hb.fit)			15.91	7756.598
00010(ha & hb.fit)			28.17	6809.348

When all other neighboring emission lines are removed, the spectrum is saved, and it is this spectrum that is used for all the other needed measurements. The images of the spectra that will be displayed will in most cases be those that have been cleaned of all their neighboring emission line components.

2.2.5 Display Transformation to Velocity Space : Centering velocity at Line center

The spectra downloaded from SDSS displays counts on the y-axis against wavelength in angstroms on the x-axis. The wavelength is logarithmic in scale. In order for us to measure the asymmetry in a clearer manner, we preferred to transform the wavelength scale to a velocity scale. This is easily done in IRAF using the command "disptrans" which is accessed in splot as well. However, since we need to measure the asymmetry, we also center the velocity at the emission line peak. This procedure displays the profile in velocity space but centered at the line peak making it possible to measure the asymmetry from the line center.

2.2.6 Spectrum Conversion to Text File : For further analysis of lines

To measure the asymmetry, there several ways one can use, some measure by hand, others prefer to use a program. In our case, we preferred to use IDL to measure asymmetry (Bowman 2005). This meant that we have to convert the spectrum image to a text file for the program to be able to read values and calculate accordingly the asymmetry. For IDL to perform this, we had to write a simple script with the necessary conditions and the desired output we needed. The output from this program are our results of the asymmetry of all the line profiles we plotted. Another advantage of converting the spectrum image to text was that we could easily plot the very image using any other plotting software like GNUplot, Python and QtiPlot (Russell & Cohn 2012; Beazley 2006; Dawson 2003; Fehily 2002; Mark 2009), making it possible to plot in any way we preferred other than the default plot of splot in Iraf.

The values or output data we obtained from the IDL program is by definition our results. By results i mean the Asymmetry Index, because from this, we can easily obtain the Kurtosis Index as well. It is the Asymmetry Index and Kurtosis Index from out data that was of prime importance from which we shall relate to other kinematic properties of the host galaxies or Ionizing regions of the AGN.

2.3 Data Treatment and Analysis

The data for our study is obtained from a series of treatment processes. The previous sections were explaining how the individual emission lines are treated in each spectrum to the moment when a text file is extracted from the fits image. This text file is convenient for further treatment and analysis since we can re-plot the emission line with any other plotting software like GnuPlot, QtiPlot and Python (Russell & Cohn 2012; Beazley 2006; Dawson 2003; Fehily 2002; Mark 2009).

Further treatment on these extracted text files is done with IDL, a program we use to extract values of the velocities at the chosen percentiles and dump them out as the useful values for further analysis. This is done for each emission line, after which a text file having all the necessary percentile velocities for all the files is obtained. It is in this file that we shall start our analysis of the asymmetry of our emission lines. In other words, this file

will contain all the information we need for each of our 447 broad Balmer emission lines in order to study the asymmetry.

Before we describe the process of extracting percentile velocities for all the emission lines, it is also necessary to briefly describe the observations made on the broad Balmer emission lines during the initial processes of obtaining the extracted individual plots.

2.3.1 Description of Obtained Data

A first analysis of the data samples showed a clear distinction between AGN with broad Balmer lines with FWHM between 1000 km/s and 3000 km/s, and those with their FWHM greater than 3000 km/s. It was observed that the former are predominantly in a lower redshift region, while the later are predominantly high red-shifted. This is evident from the fact that out of 80 spectra in the first sample, 67 contained both broad Balmer emission lines, while for sample 2, out of 200 spectra, 98 contained both emission lines, the others missing the $H\alpha$ emission line due to being red-shifted.

From figures 9 and 10, we can notice that sample 2 is clearly unbiased in its redshift distribution as sample 1 is.

2.3.2 Other levels of the data

The data obtained initially is in the form of spectroscopic data, spectra downloaded from $SDSSDR7$ from which the asymmetry is measured using the IDL script we developed (Bowman 2005). The asymmetry values are then used to obtain the steepness of the profiles.

In order to relate the asymmetry and kurtosis to other kinematic properties, we needed to obtain more data pertaining the objects whose values of asymmetry and kurtosis we have. This other data includes:

- Flux values of [OIII], [OII] & [OI] for obtaining the ionization degrees through their flux ratios.
- V-Band magnitudes for calculating the Luminosity.
- Radio Flux measurements for those sources whose radio fluxes have been databased already.
- Line width values of $H\alpha$ and $H\beta$ emission lines.

Values of the flux of the oxygen lines were obtained from the downloaded spectra. This was not an easy task as quite a number of sources were red-shifted in such a manner that either [OI] was missing or [OII] was missing. However, it was still possible to have objects in which we could obtain values from both emission lines.

The V-Band magnitudes were obtained using an sql script, which we wrote, to download spectroscopic values of $ugriz$ photometry data, from which i transformed the values to the $UBVRcIc$ system. The V-Band magnitude was then calculated as:

$$V = g - 0.58 * (g - r) - 0.01 \qquad (11)$$

It then made it possible to transform the magnitude to Luminosity.

Radio flux values were obtained from the NASA/IPAC EXTRAGALACTIC DATABASE, in which i inputted the coordinates of all my sources. The query returned all the sources whose radio flux was databased. The radio flux was in milliJansky. Also to note is that since we are interested in the core radio flux, the radio flux measurements queried were for regions within a 5.0 arc-sec cone.

All the different sets of data were synchronized to match the asymmetry and kurtosis

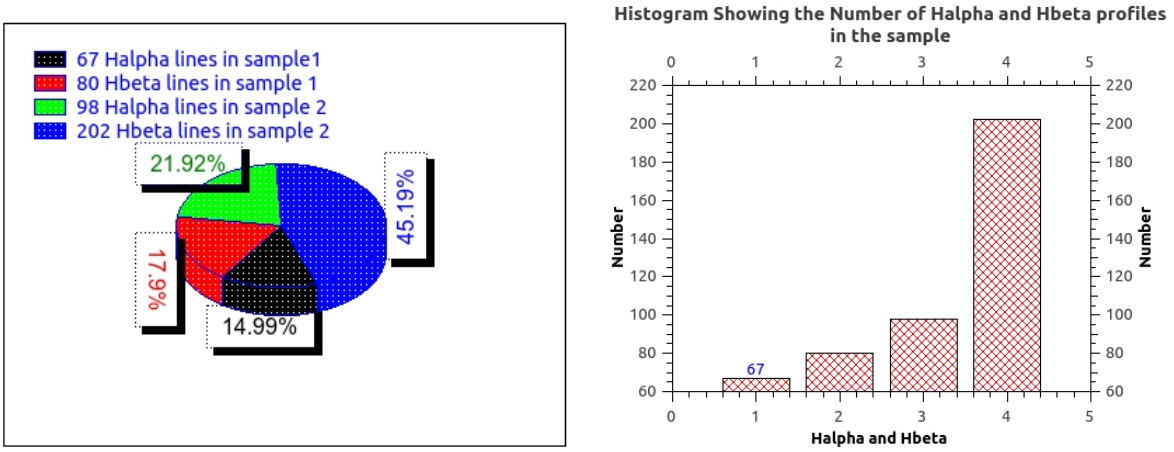


Figure 8: A pie chart and bar graph showing the distribution of both $H\alpha$ and $H\beta$ emission lines in the sample

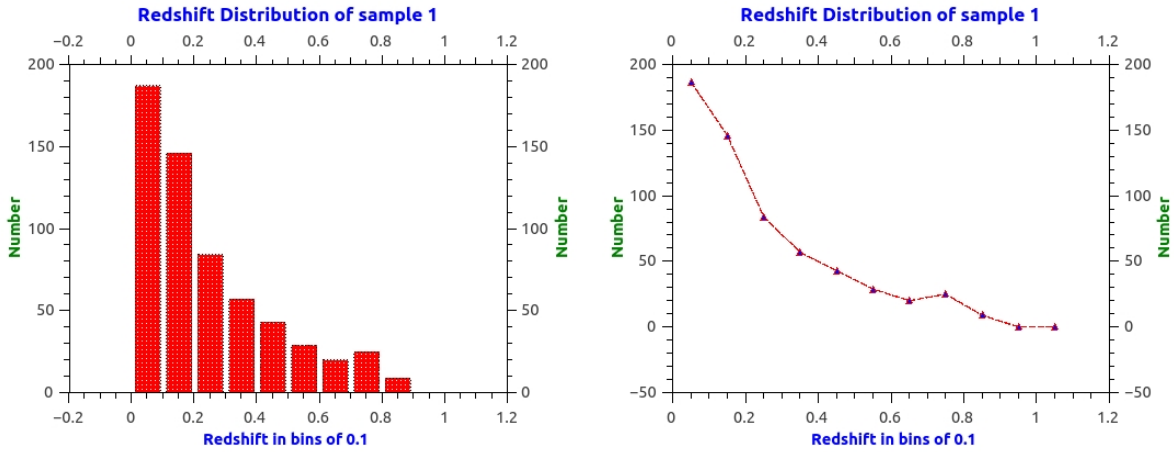


Figure 9: Redshift distribution of sample 1

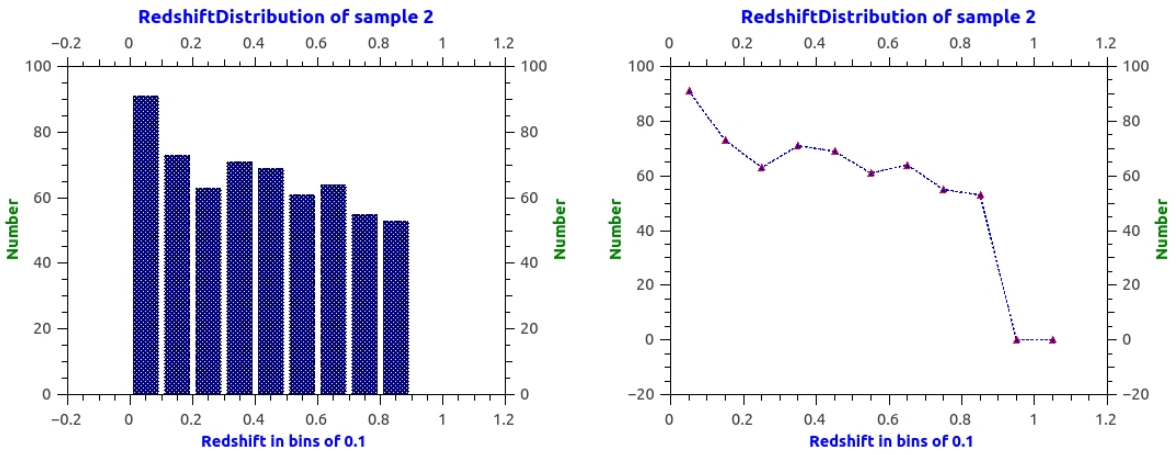


Figure 10: Redshift distribution of sample 2

values for analysis. To note too is that the data was separated in two sets; that of $H\alpha$ profiles and that of $H\beta$ profiles. In the analysis to follow, it will be noted that plots of $H\alpha$ and $H\beta$ are placed besides each other, with the $H\alpha$ to the left and $H\beta$ to the right, where possible in different colors as well.

2.3.3 Plotting

Plotting in this work is done using quite a number of programs, from IDL (Bowman 2005), QtiPlot (Russell & Cohn 2012) and Python (Beazley 2006; Dawson 2003; Fehily 2002; Mark 2009). However, most of the plots in the Data section are plotted using Python, where made a script for each dataset so that it minimizes the size of the text file containing the data. It is beyond the scope of this section to give more details of the scripts. However, a sample will be attached in the Appendix section for more clarification. The reasons for using various programs to plot ranged from which type of plot was needed and which data i was analyzing as i always used the most efficient one for each type of plot i needed.

3 Results

In this section, we present the results obtained from the data analysis and a discussion about them. By results here, we focus on the Asymmetry Index and Kurtosis Index of the Balmer emission lines measured. We analyze the distribution of the Asymmetry Index across the whole profile from FWZI to its peak. In the later half of the chapter, we relate the Asymmetry Index to other kinematic properties such is ionization degree (De Robertis & Shaw 1990; Padovani & Rafanelli 1988), radio flux (Brotherton 1996), luminosity and the line width (FWHM) (Yu & Gan 2006).

3.1 Distribution of results

On obtaining the Asymmetry Index and Kurtosis Index, it was necessary to briefly show how they are distributed. We chose to plot a frequency distribution of the Asymmetry Index and Kurtosis index.
The Asymmetry Index varies from -1 to +1, a value of 0 meaning the profile is symmetric while a deviation to either side of the zero implies asymmetry. The degree of asymme-

try in each case will be probed by relating to other kinematic properties. It is to our interest to find out whether this positive asymmetry and kurtosis is related to either non-thermal or thermal radiation and/or even to the relative strength and kinematics of the BLR. If the degree of asymmetry is a measure of the radial flow of material from or to the BLR, then it will be possible to understand the structure of the accretion disk winds using asymmetry index.

In our distributions to follow, we separate the $H\alpha$ emission line profile asymmetry from that of the $H\beta$ emission lines. The Kurtosis Index follows the same pattern.

3.2 Asymmetry Index

The values obtained from the IDL script yielded values of the Asymmetric Index for both the $H\alpha$ emission lines and $H\beta$ emission lines. The bar graphs that follow reproduce the statistical distribution of the Asymmetry Index for both Balmer lines, with the $H\alpha$ on the left of each double image figure (in blue) and $H\beta$ to the right (in green).

It is also important to review the meaning of a value of asymmetry index as seen on the plots. This is seen in 2 below

Fig 11 shows the Asymmetry Index distribution of $H\alpha$ emission lines, on the left hand, and $H\beta$ emission lines, in the right side at FW20%I. It is noticed that the AI is almost symmetric and peaking in the red end for $H\alpha$ but still red-shifted for $H\beta$.

Fig 12 shows the Asymmetry Index distribution of $H\alpha$ emission lines, on the left hand, and $H\beta$ emission lines, in the right side at FW30%I. It is noticed that the AI is almost symmetric for $H\alpha$ but still red-shifted for $H\beta$.

Fig 13 shows the Asymmetry Index distribution of $H\alpha$ emission lines, on the left hand, and $H\beta$ emission lines, in the right side at FW40%I. It is noticed that the AI is almost symmetric for $H\alpha$ but still red-shifted for $H\beta$.

Fig 14 shows the Asymmetry Index distribution of $H\alpha$ emission lines, on the left hand, and $H\beta$ emission lines, in the right side at FW50%I. It is noticed that the AI is almost symmetric for $H\alpha$ but still red-shifted for $H\beta$.

Fig 15 shows the Asymmetry Index distribution of $H\alpha$ emission lines, on the left hand, and $H\beta$ emission lines, in the right side at FW60%I. It is noticed that the AI is almost symmetric for $H\alpha$ but still red-shifted for $H\beta$.

Fig 16 shows the Asymmetry Index distribution of $H\alpha$ emission lines, on the left hand, and $H\beta$ emission lines, in the right side at FW70%I. It is noticed that the AI is almost symmetric for $H\alpha$ but still red-shifted for $H\beta$.

A few key features are noticed here, $H\alpha$ profiles are almost symmetric, they tend to peak in the red end but the degree of asymmetry is negligible. For the $H\beta$ profiles, it is noticed that most of them are clearly asymmetric, peaking predominantly in the positive side. This is maintained all through the profile from the base, FWZI, to the core of the profile at the higher percentiles.

A sample of symmetric profiles can be seen in figures 17 for $H\alpha$ profiles and 19 for the $H\beta$ profiles. Asymmetric profiles can be seen in figures 18 and 18 for the $H\alpha$ and $H\beta$ emission lines respectively. It is evident that the $H\beta$ profiles display the highest degree of asymmetry.

3.3 Kurtosis Index

The Kurtosis Index is a measure of how steep the profile is. The Kurtosis parameters are all less than unity, with a decrease in value indicating an increase in steepness. The parame-

Table 2: Interpretation of Asymmetry Index

Asymmetry Index (x)	Measure	Interpretation
$0<x \leq 0.08$	Weak	The distribution is relatively symmetrical.
$0.08<x \leq 0.15$	Moderate	The distribution is relatively asymmetrical.
$x>0.15$	Strong	The distribution is asymmetrical.

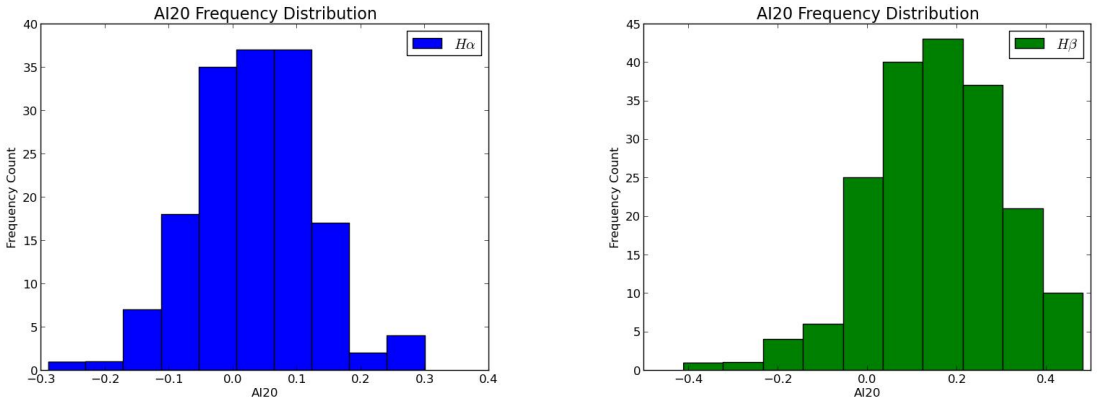


Figure 11: Frequency Distribution of the AI20 of $H\alpha$ and $H\beta$ emission line profiles

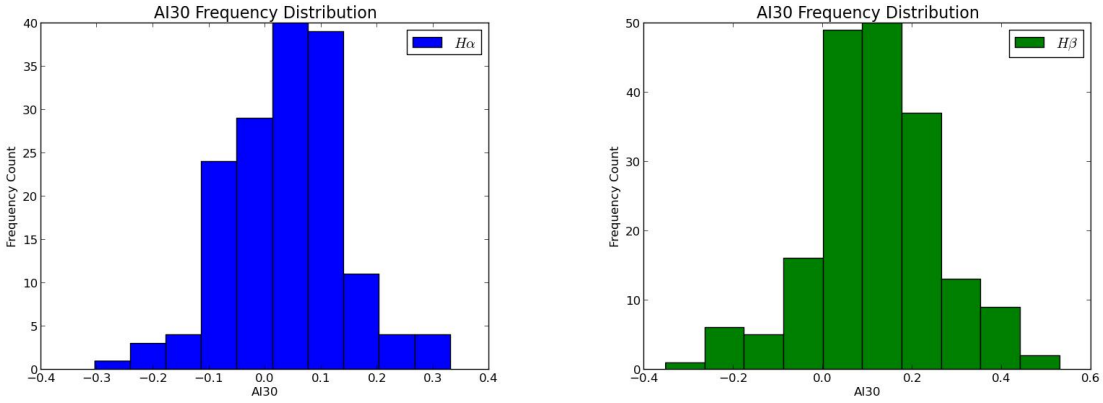


Figure 12: Frequency Distribution of the AI30 of $H\alpha$ and $H\beta$ emission line profiles

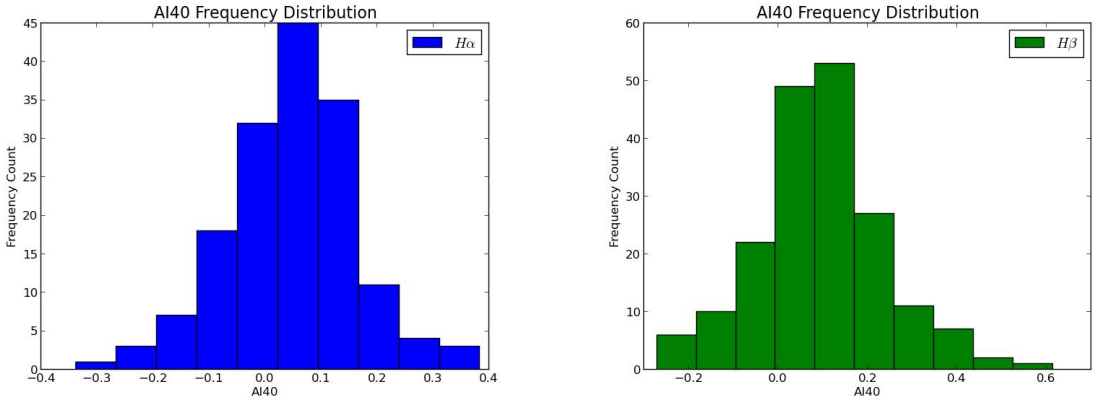


Figure 13: Frequency Distribution of the AI40 of $H\alpha$ and $H\beta$ emission line profiles

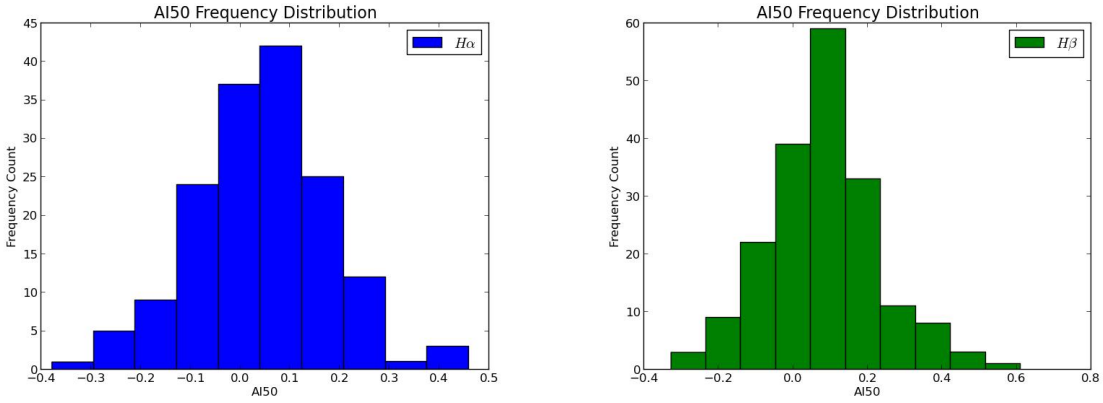


Figure 14: Frequency Distribution of the AI50 of $H\alpha$ and $H\beta$ emission line profiles

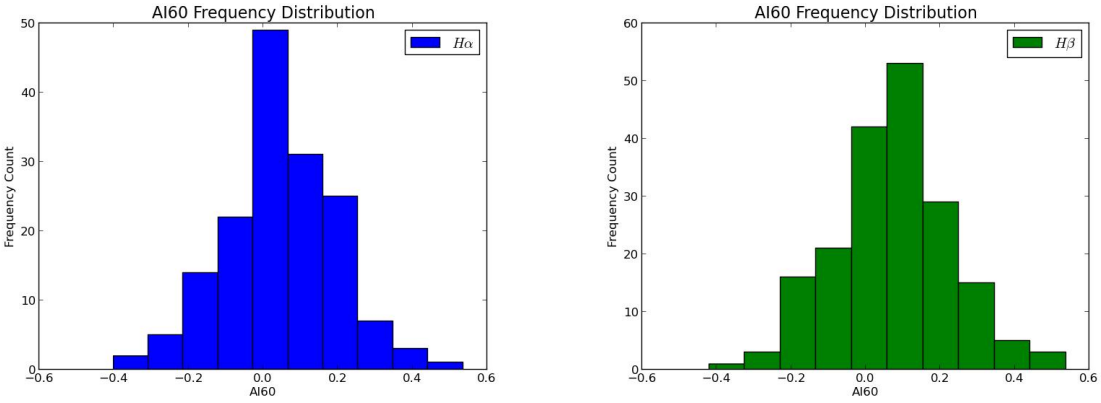


Figure 15: Frequency Distribution of the AI60 of $H\alpha$ and $H\beta$ emission line profiles

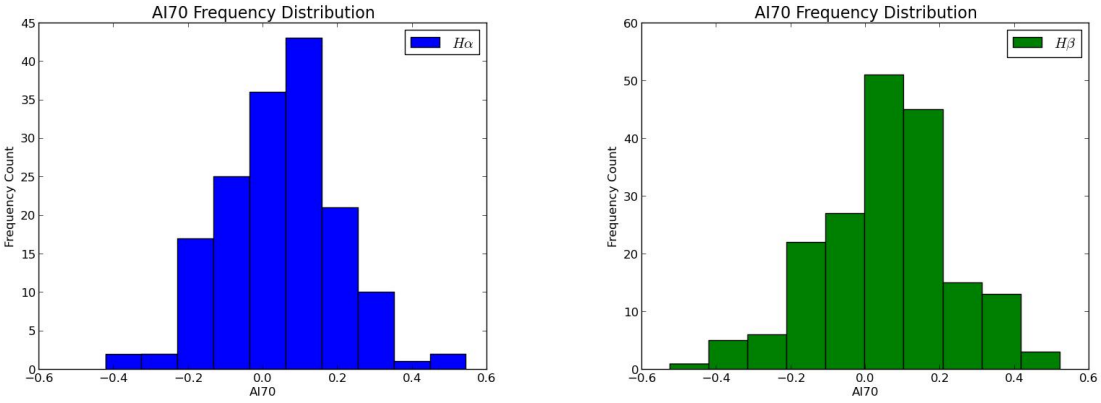


Figure 16: Frequency Distribution of the AI70 of $H\alpha$ and $H\beta$ emission line profiles

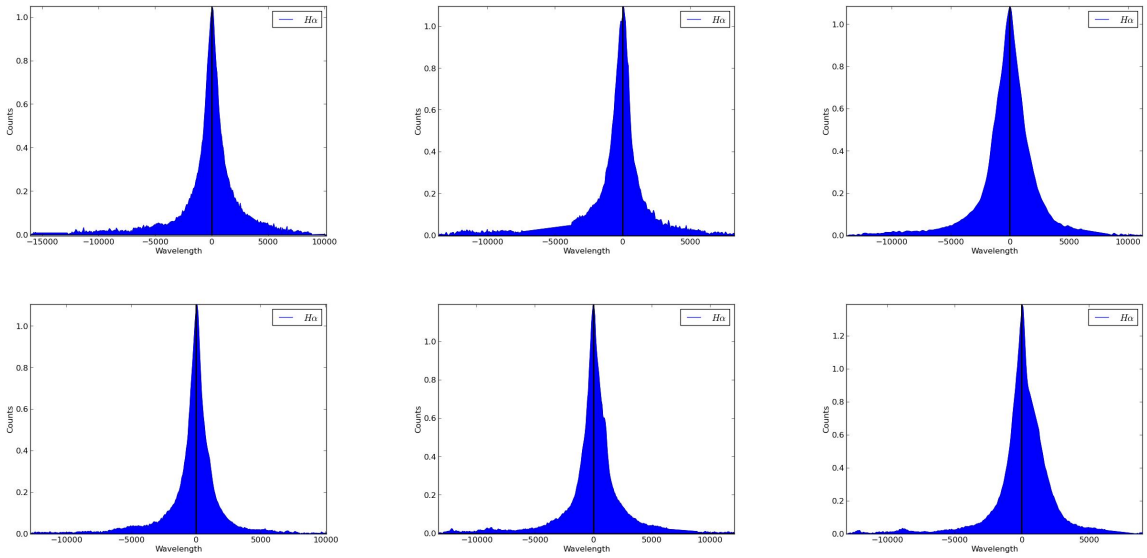


Figure 17: Some examples of symmetric $H\alpha$ line profiles

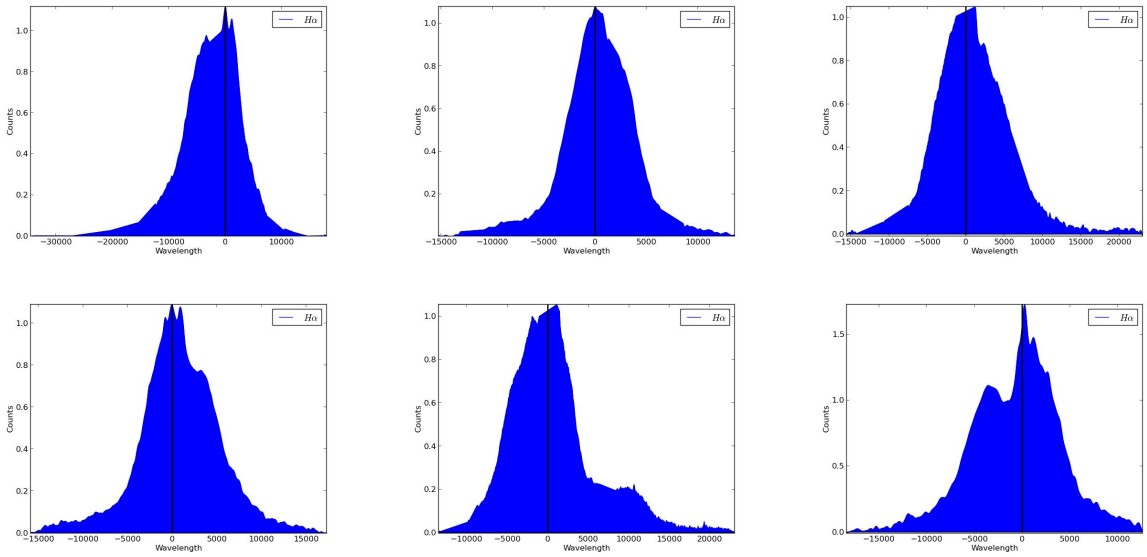


Figure 18: Some examples of asymmetric $H\alpha$ line profiles

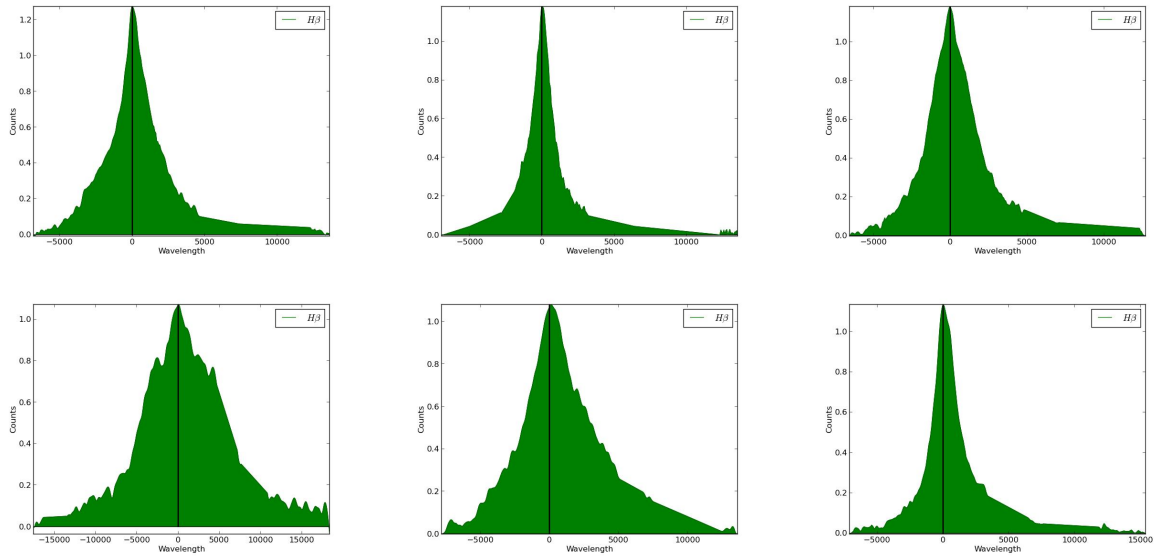


Figure 19: Some examples of symmetric $H\beta$ line profiles

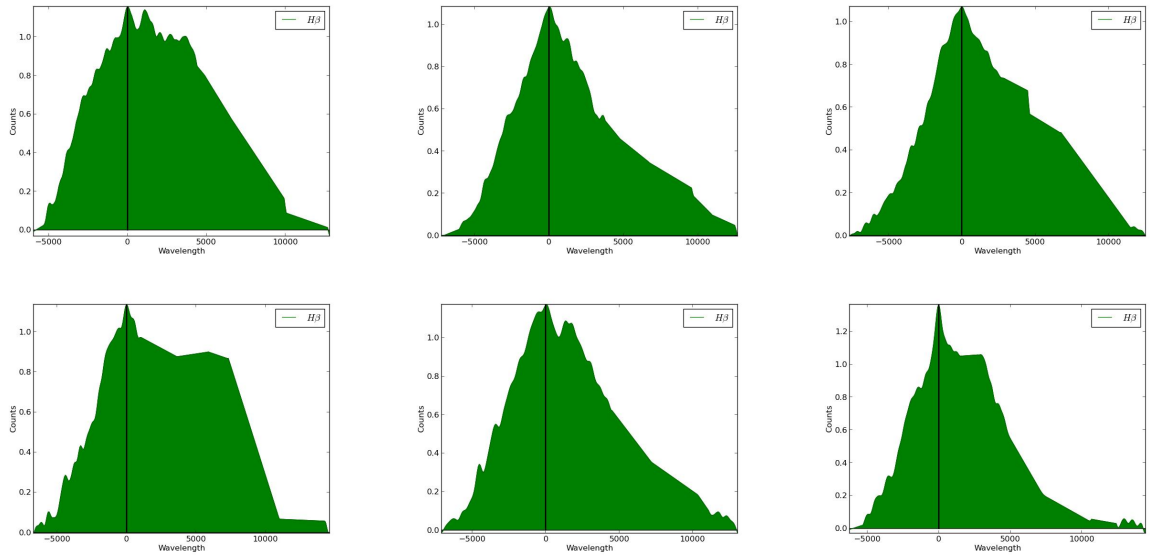


Figure 20: Some examples of asymmetric $H\beta$ line profiles

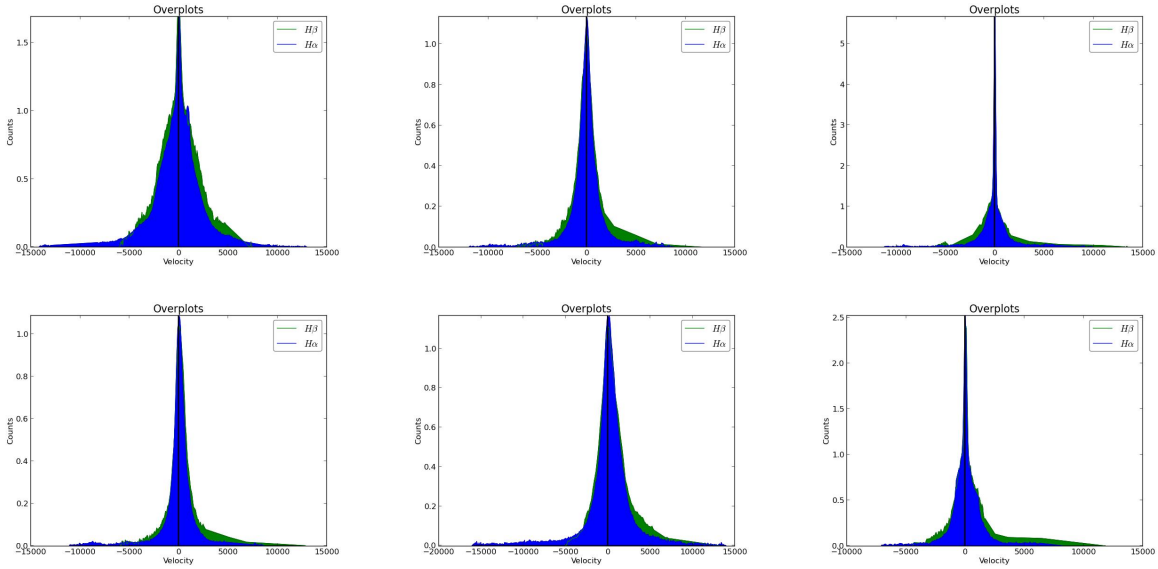


Figure 21: Some examples of symmetric $H\alpha$ and $H\beta$ line profiles overploted

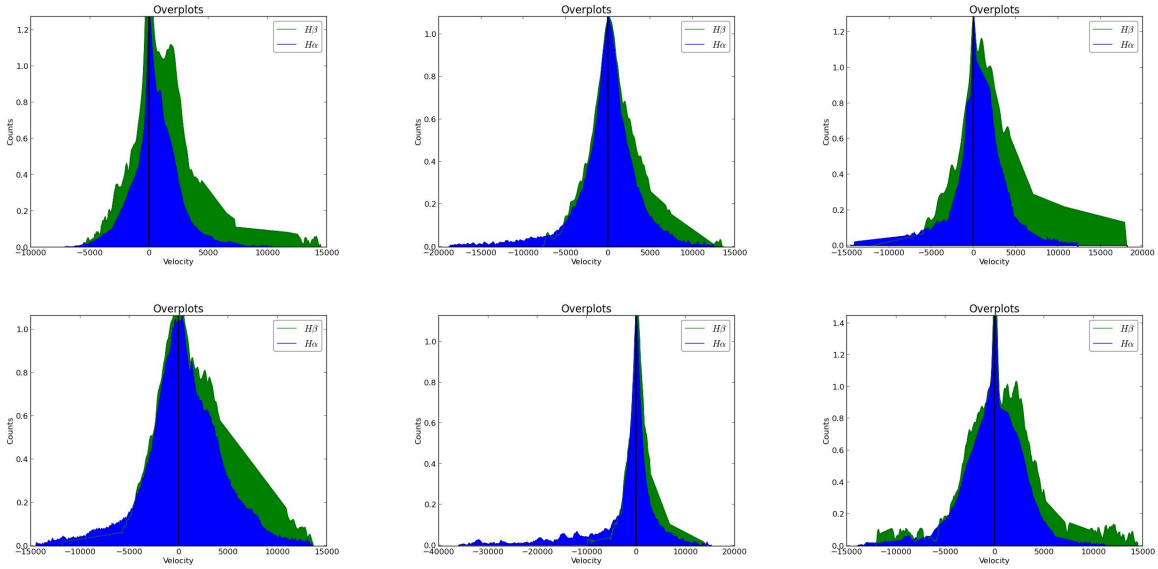


Figure 22: Some examples of asymmetric $H\alpha$ and $H\beta$ line profiles overploted

ters will range from 0.0 to 1.0, but of course with very few profiles having values close to 1.0. (Whittle 1985a)
Table 3 shows an overview of the Kurtosis parameters and their meaning.

For the Kurtosis parameters, it is vital to note that this is a measure of how the profile shape changes from the top to the bottom. A value of close to unity signifies almost no change in the steepness. A value close to zero on the other hand will mean a very large change in the shape as one moves towards the base of the profile. This means the profile shape rapidly changes from narrow to broad. Some profiles may be broad but with low values of Kurtosis, that is if they are consistently broad from the upper part of the emission line to below the half maximum. Profiles that show this shape are mostly those in which the narrow component is not available or obscured. There are other broad emission line profiles that will display high values of Kurtosis, that is, having significantly extended wings. It is also noted that high values of asymmetry in a profile suffice low values in Kurtosis.

In dealing with the Kurtosis measure, three regions of the profile are chosen, the top measured with KI_1, the middle, measured with KI_2, and the bottom, measured with KI_3. Thus each of these values shows a change in profile in the mentioned regions on the overall profile. To capture the whole profile, another parameter is defined, KI_{Gen}, which measures the overall change in shape of the profile from the top to the bottom.

Figures 23, 24, 25 and 27 show the change in profile shape of the $H\alpha$ and $H\beta$ profiles, with the ones to the left (in red) for $H\alpha$ and the ones to the right (in blue) for the $H\beta$ profiles.

It is shown in fig 23 that the change in profile shape for the top parts of the $H\alpha$ and $H\beta$ emission lines is quite high, peaking at values close to 0.25.

Fig 24 shows that the change in profile shape for the center parts of the $H\alpha$ and $H\beta$ emission lines is moderate, peaking at values close to 0.6.

Fig 25 shows that the change in profile shape for the lower parts of the $H\alpha$ and $H\beta$ emission lines is low, peaking at values close to 0.8.

The three measures of steepness, KI_1, KI_2 and KI_3 show a pattern in profile shape change. The change in shape breaks down as one moves to the base. This can be an indication of a systematic change to Lorentzian from Gaussian, as the change should be smooth as one moves from around 60% of the profile downwards. One cannot expect an abrupt change from Gaussian to Lorentzian. It could also be due to the selection of the regions of low, center and bottom. Looking at only two regions, top and bottom, breaks the smooth transition since the measure of the center of the profile reflects the effects from the same physical conditions as the lower part of the profile as can be seen in 26.

Fig 27 shows that the change in overall profile shape of the $H\alpha$ and $H\beta$ emission lines is moderate, peaking at values close to 0.55.

The general trend of profile shape change is expected as not so many sources show high asymmetries, but the mere fact that there are some sources in the distribution with high measures in asymmetry and low measures in kurtosis justifies the study. It is now clearly vital to proceed and look up other kinematic properties and find out which of them correlate with the high values of asymmetry and low values of Kurtosis. A previous study on 90 emission line profiles,constituting 30 Balmer lines and 55 forbidden and 5 other permitted lines, from 31 objects comprising of S1, S2, S3 classes of Seyfert galaxies, H

Table 3: Interpretation of Kurtosis Index

Kurtosis Index (x)	Measure	Interpretation
$0<x \leq 0.25$	Strong	The change in shape is very large.
$0.25<x \leq 0.65$	Moderate	The change in shape is normal.
$x>0.65$	Weak	The change in shape in insignificant.

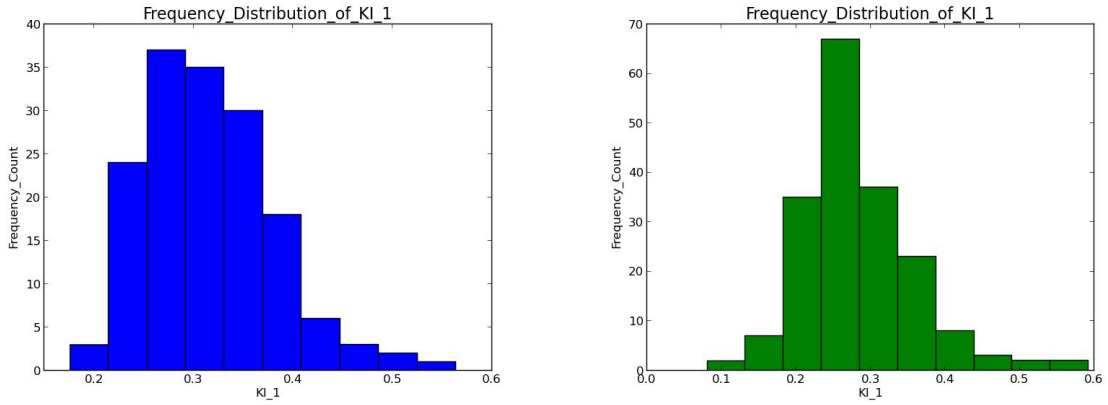


Figure 23: Frequency Distribution of the KI 1 of $H\alpha$ and $H\beta$ emission line profiles

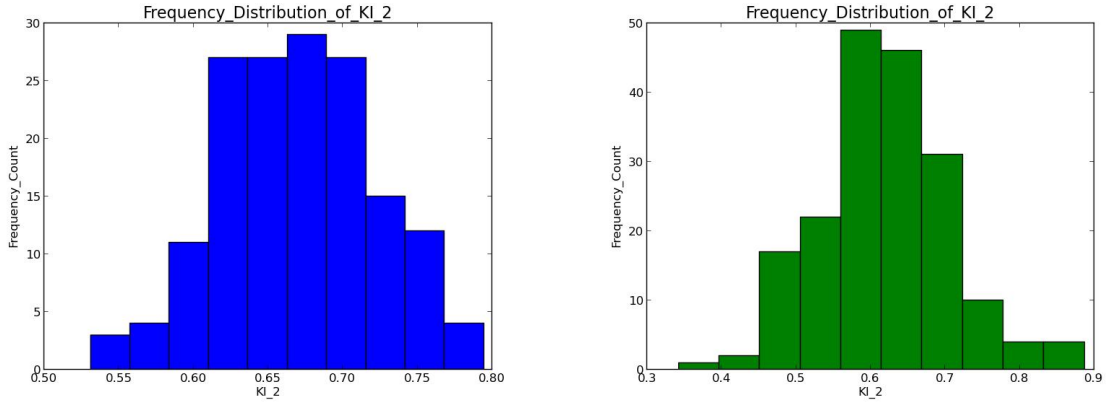


Figure 24: Frequency Distribution of the KI 2 of $H\alpha$ and $H\beta$ emission line profiles

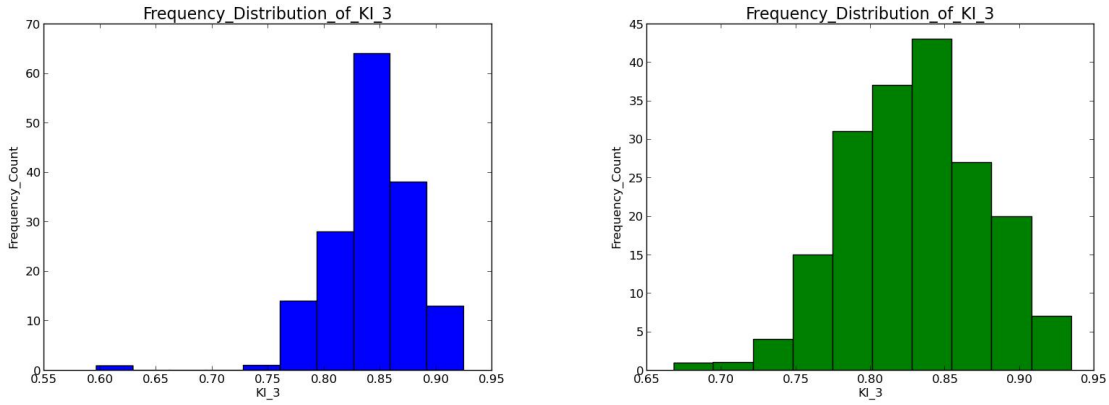


Figure 25: Frequency Distribution of the KI 3 of $H\alpha$ and $H\beta$ emission line profiles

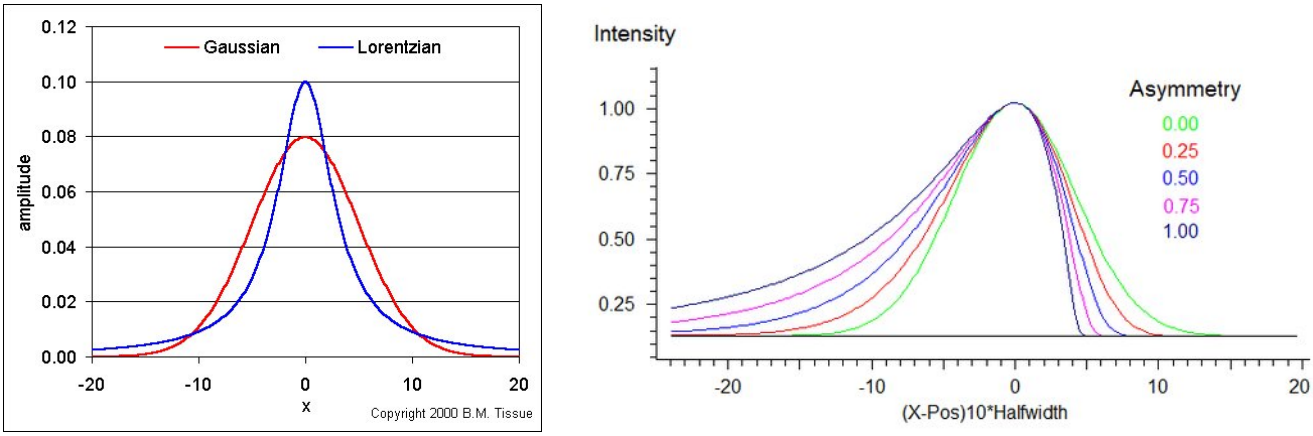


Figure 26: Images Showing the percentiles used to calculate values of Kurtosis and Asymmetry.

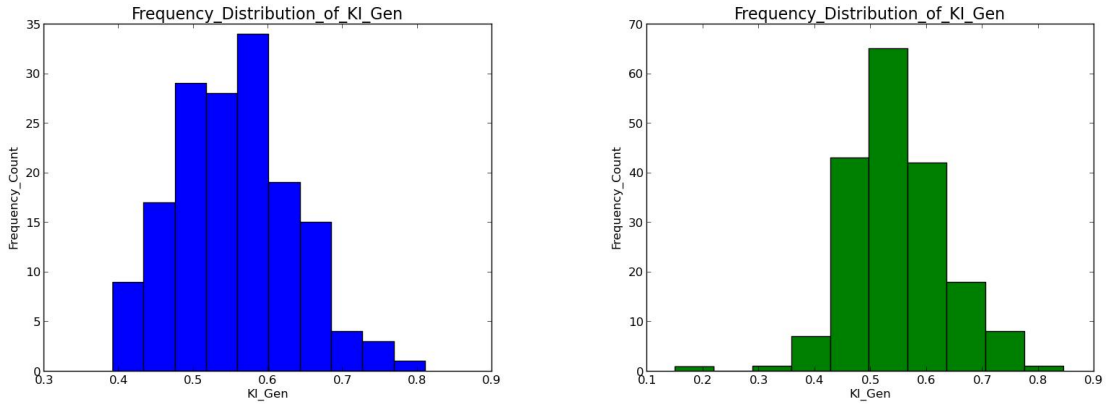


Figure 27: Frequency Distribution of the KI Gen of $H\alpha$ and $H\beta$ emission line profiles.

II regions and QSOs showed that Forbidden lines are found to be narrower and steeper, while Balmer lines and other permitted lines are broader and flatter (Basu 1994), meaning that the Kurtosis measure will be small as we also observed in the KI_1.

3.4 Asymmetry Index relation to other kinematic properties

While we have the Asymmetry Index and Kurtosis Index, its scientifically worthwhile to relate this measure to some other kinematic properties (Whittle 1985b). Some of the properties we related Asymmetry Index to are; the FWHM, the luminosity in the V-Band, the Radio Flux, and Ionization degree using the Oxygen narrow emission lines.

3.4.1 Relation of Asymmetry Index to the Line Width(FWHM)

The Line width is a measure of the strength of the spectral properties in the source which can be used to obtain a number of estimates about the size, radius of the region. A relation of this measurement with line asymmetry is important in the quest to obtain the origin of the asymmetry and the nature of the mechanism. Thus the asymmetry here will play a great deal in probing the flow of material in and out of the BLR. This is in line with the relation here as the base of the profiles shows high asymmetries, thus more effects from the motions of the material than in the upper portions of the profile. This is a general trend, which is in agreement with the underlying physics. We also study individual relations with each percentile in the plots that follow.

The following ten plots are relations of Asymmetry Index and FWHM, those to the left are of $H\alpha$ (in green) while those to the right are for $H\beta$ (in blue).

In Fig30, the relation between the FWHM and AI20 is shown. The $H\alpha$ does not appear to have a relation with the two variables, the points are heavily scattered in the plotBut also the relation observed with the $H\beta$ tends to start breaking down from previous relations. We observe an increase in asymmetry with line width.

Figures 31, 32, 33 and 34 all show a decrease in line width with asymmetry for $H\alpha$ and an increase in line width with asymmetry

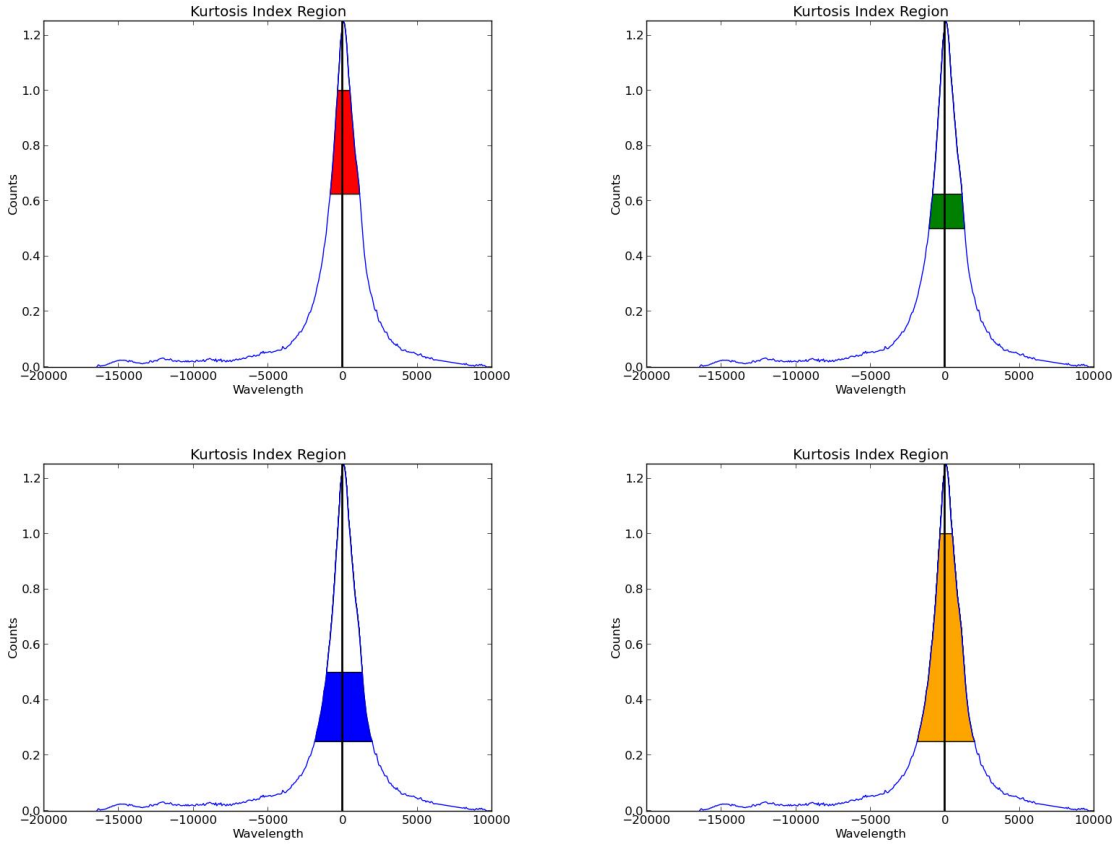


Figure 28: Kurtosis Index Regions for the Steep Profiles

Table 4: Correlation Coefficients for Line Width Verses $H\alpha$ Asymmetry

Percentile	ρ_p	$P_p - value$	ρ_s	$P_s - value$	ρ_k	$P_k - value$	m	b
20	-0.0338	0.6661	-0.0235	0.7642	-0.0155	0.7673	-0.0838	3.5049
30	-0.1500	0.0545	-0.1319	0.0914	-0.0896	0.0877	-0.3372	3.5151
40	-0.1604	0.0396	-0.1627	0.0368	-0.1076	0.0402	-0.3227	3.5162
50	-0.1507	0.0533	-0.1512	0.0525	-0.1032	0.0492	-0.2620	3.5137
60	-0.1323	0.0903	-0.1220	0.1185	-0.0878	0.0941	-0.2036	3.5110
70	-0.1004	0.1996	-0.0889	0.2559	-0.0627	0.2321	-0.1459	3.5082

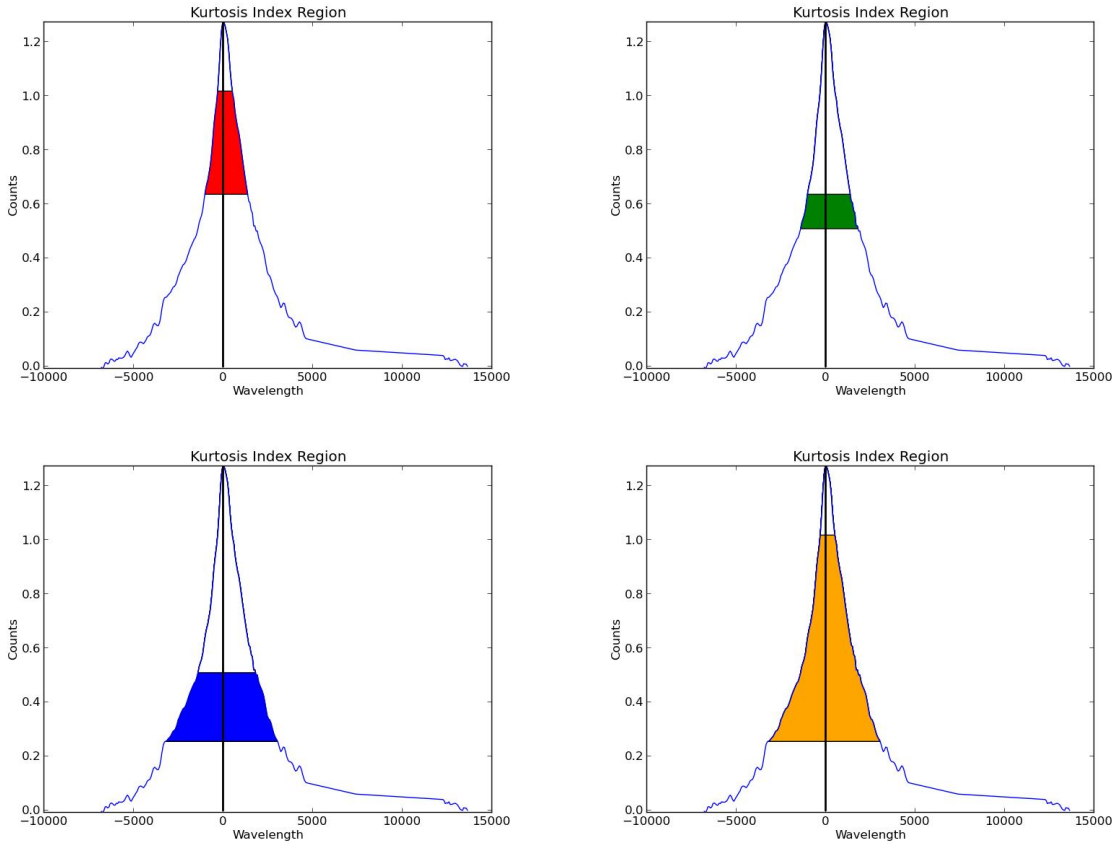


Figure 29: Kurtosis Index Regions for the Flatter Profiles

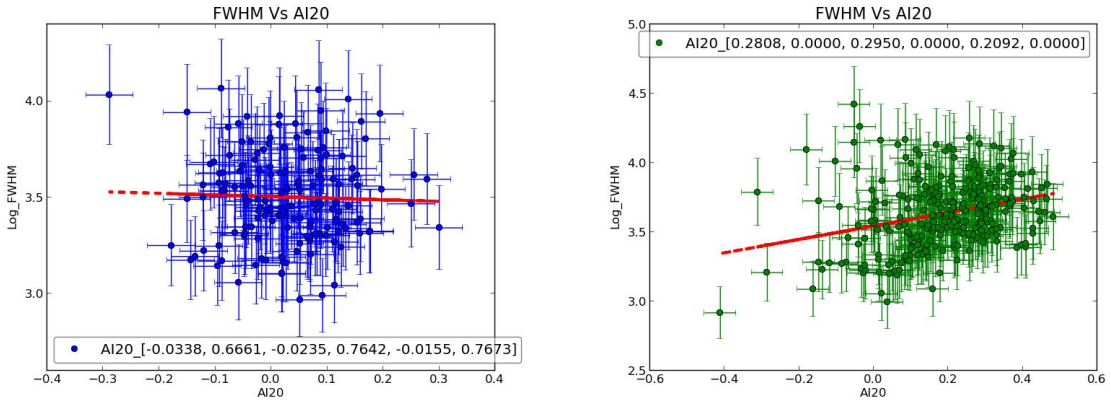


Figure 30: Relation of the AI20 of $H\alpha$ and $H\beta$ emission line profiles with Line width

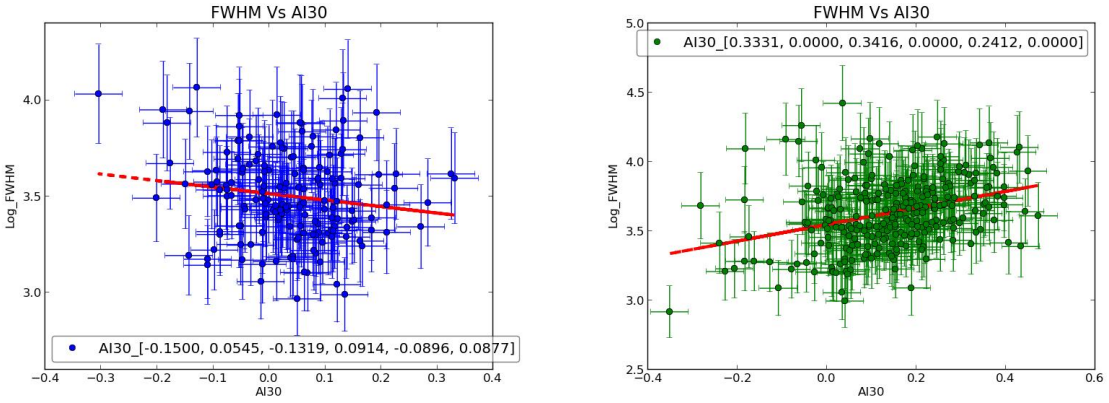


Figure 31: Relation of the AI30 of $H\alpha$ and $H\beta$ emission line profiles with Line width

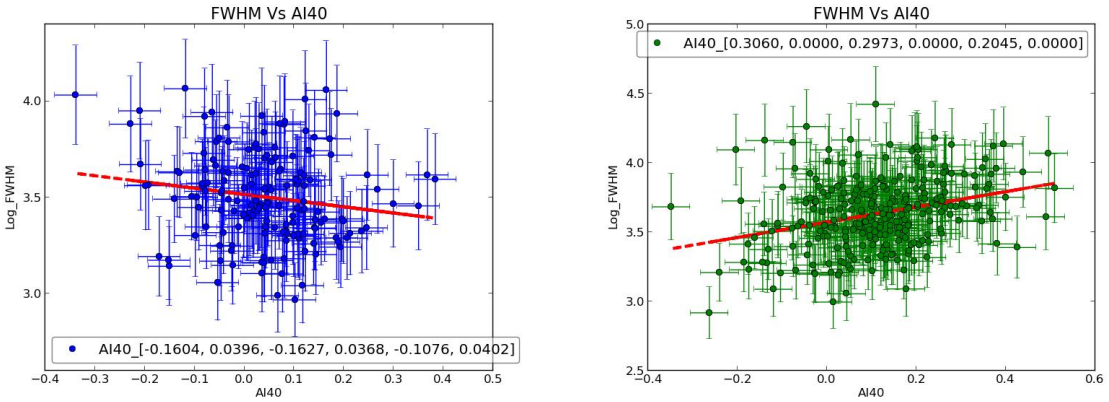


Figure 32: Relation of the AI40 of $H\alpha$ and $H\beta$ emission line profiles with Line width

Table 5: Correlation Coefficients for Line Width Verses $H\beta$ Asymmetry

Percentile	ρ_p	$P_p-value$	ρ_s	$P_s-value$	ρ_k	$P_k-value$	m	b
20	0.2808	0.0000	0.2950	0.0000	0.2092	0.0000	0.4842	3.5448
30	0.3331	0.0000	0.3416	0.0000	0.2412	0.0000	0.5977	3.5481
40	0.3060	0.0000	0.2973	0.0000	0.2045	0.0000	0.5515	3.5719
50	0.2536	0.0000	0.2272	0.0001	0.1519	0.0002	0.4338	3.5919
60	0.2001	0.0008	0.1622	0.0066	0.1085	0.0069	0.3283	3.6045
70	0.1218	0.0421	0.1010	0.0921	0.0686	0.0876	0.1787	3.6210

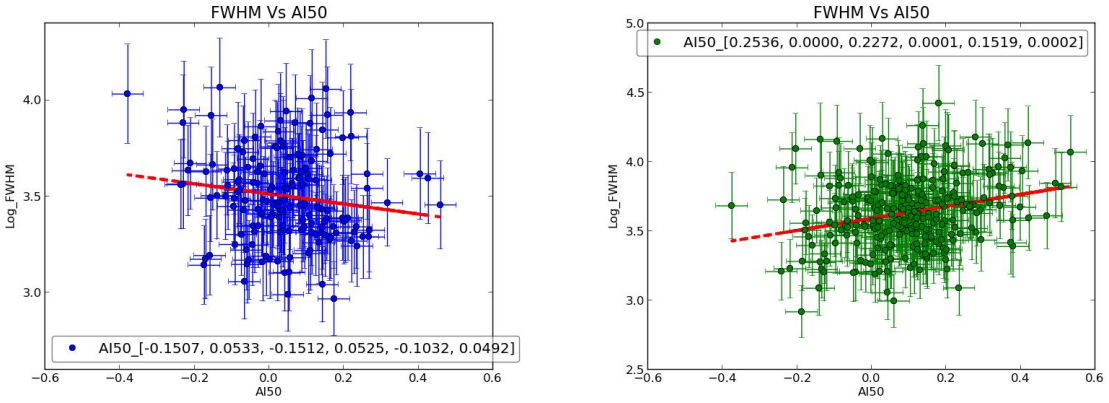


Figure 33: Relation of the AI50 of $H\alpha$ and $H\beta$ emission line profiles with Line width

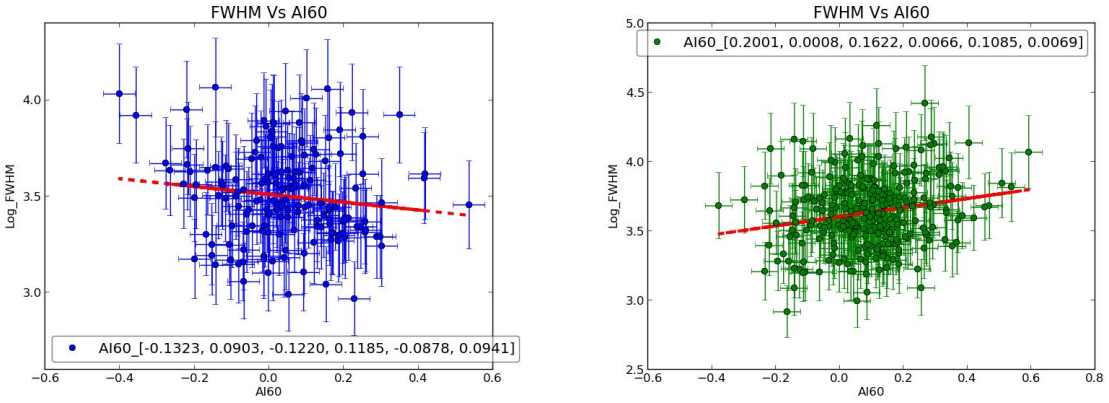


Figure 34: Relation of the AI60 of $H\alpha$ and $H\beta$ emission line profiles with Line width

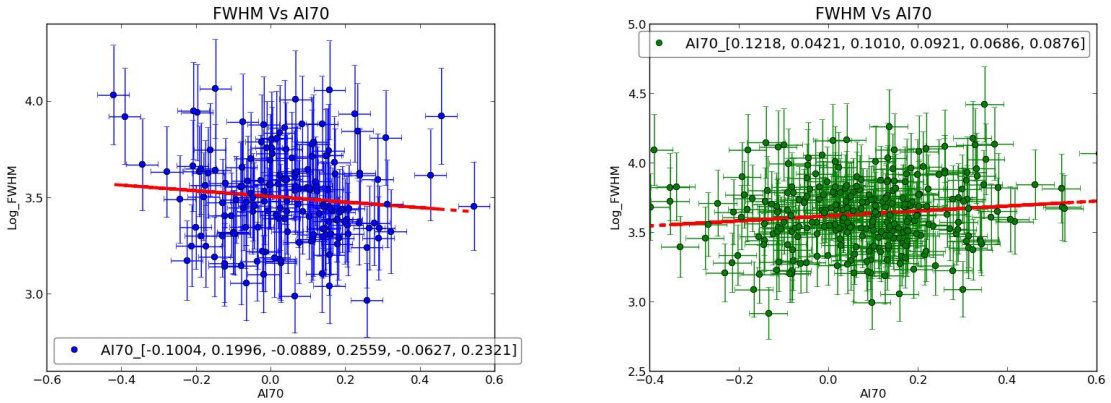


Figure 35: Relation of the AI70 of $H\alpha$ and $H\beta$ emission line profiles with Line width

with $H\beta$.

In a nutshell, excluding the FWZI, all $H\alpha$ profile percentiles display a negative correlation while $H\beta$ profiles display positive correlations excluding their 00% and 90% percentile. The later correlations are tighter making the $H\beta$ shape parameters better at analyzing effects causing profile shape in Balmer emission lines. It is also a reflection from the previous statistic on the distribution of asymmetry index where we observed that the $H\beta$ profiles displayed more positive asymmetry as opposed to the $H\alpha$ profiles that were statistically symmetric.

3.4.2 Relation of Asymmetry Index to the V Band Luminosity

The relationship of Luminosity with the asymmetry of broad Balmer lines is of great importance because luminosity of one of the properties that can easily be obtained from a source. Having a clear relationship with this property will help in further scientific relationships with the AGN Broad Line Region physics. Since the luminosity has already existing relationships with parameters like Black Hole mass, accretion rate and morphological type, it will help us relate asymmetry of profiles to all there other properties of the galaxies. One excellent correlation is that between the Black Hole mass and Optical luminosity obtained by Peterson et al. (2004). It was observed that Black Hole mass increased with optical luminosity. The correlation between asymmetry and V-Band luminosity therefore will also help us in probing this further. Kaspi et al. (2002) also found a tight correlation between the luminosity and the radius of the BLR. This will also help is relate our asymmetry with the radius of the BLR. The preceding relations are also divided into two, the relation to the left being that of $H\alpha$ profiles and that to the right being that of the $H\beta$ profiles. But generally, there seems not to be direct relationships between these parameters apart from that of AI00.

In all the relations of Luminosity with asymmetry, it is observed right from figure 36 through to 41 that the $H\alpha$ asymmetry relations are non-existent or very weak, if found. However, the asymmetry in $H\beta$ is observed to be consistent apart from the first and last percentiles. $H\beta$ positive asymmetry is observed to rise with increasing Luminosity. Increasing luminosity correlates with increasing BLR ra-

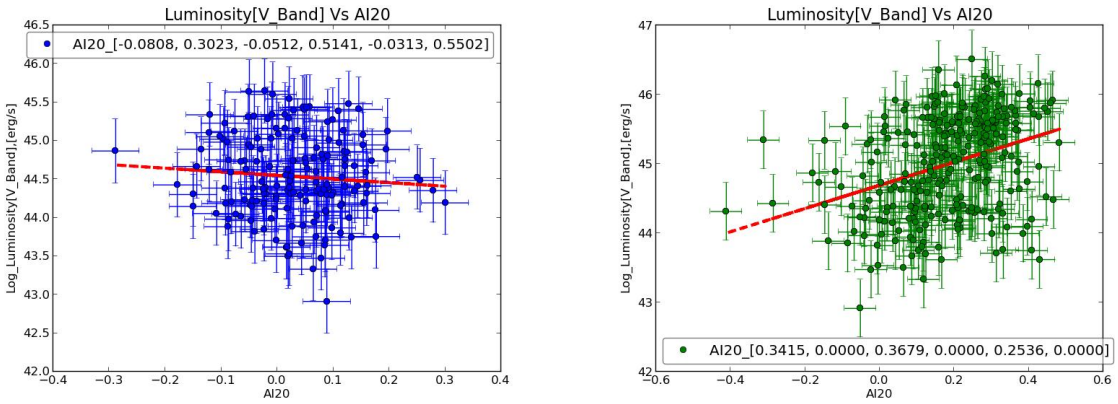


Figure 36: Relation of the AI20 of $H\alpha$ and $H\beta$ emission line profiles with V Band Luminosity

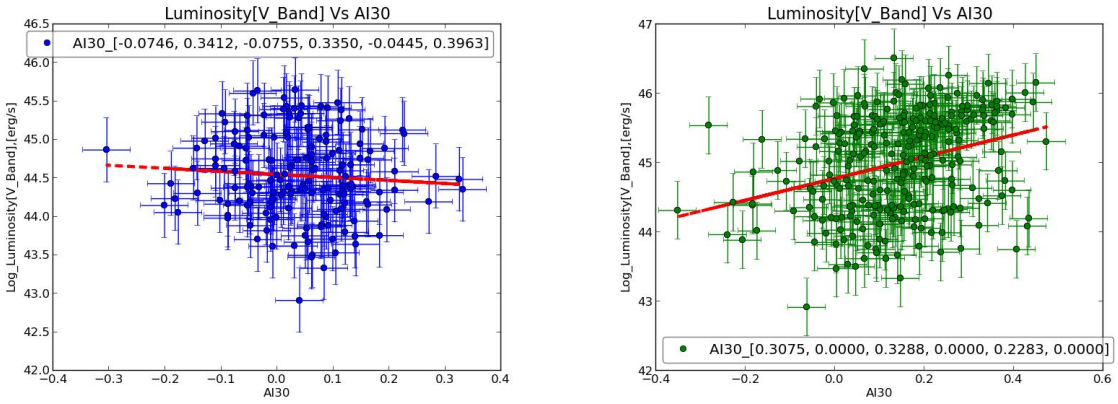


Figure 37: Relation of the AI30 of $H\alpha$ and $H\beta$ emission line profiles with V Band Luminosity

Table 6: Correlation Coefficients for V-Band Luminosity Verses $H\alpha$ Asymmetry

Percentile	ρ_p	$P_p-value$	ρ_s	$P_s-value$	ρ_k	$P_k-value$	m	b
20	-0.0808	0.3023	-0.0512	0.5141	-0.0313	0.5502	-0.4690	44.5500
30	-0.0746	0.3412	-0.0755	0.3350	-0.0445	0.3963	-0.3932	44.5504
40	-0.0763	0.3302	-0.0863	0.2705	-0.0534	0.3090	-0.3599	44.5510
50	-0.0897	0.2521	-0.0885	0.2585	-0.0584	0.2656	-0.3655	44.5515
60	-0.0898	0.2511	-0.0941	0.2294	-0.0593	0.2584	-0.3243	44.5494
70	-0.0548	0.4849	-0.0599	0.4449	-0.0368	0.4828	-0.1867	44.5431

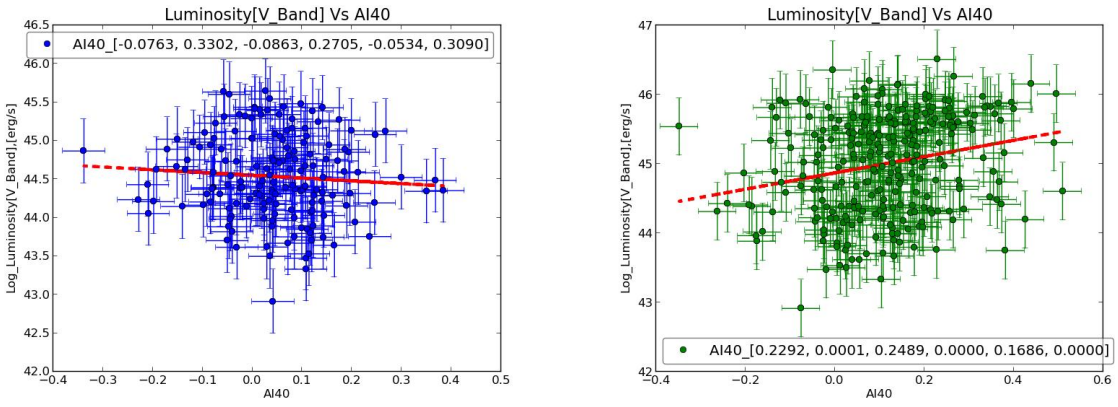


Figure 38: Relation of the AI40 of $H\alpha$ and $H\beta$ emission line profiles with V Band Luminosity

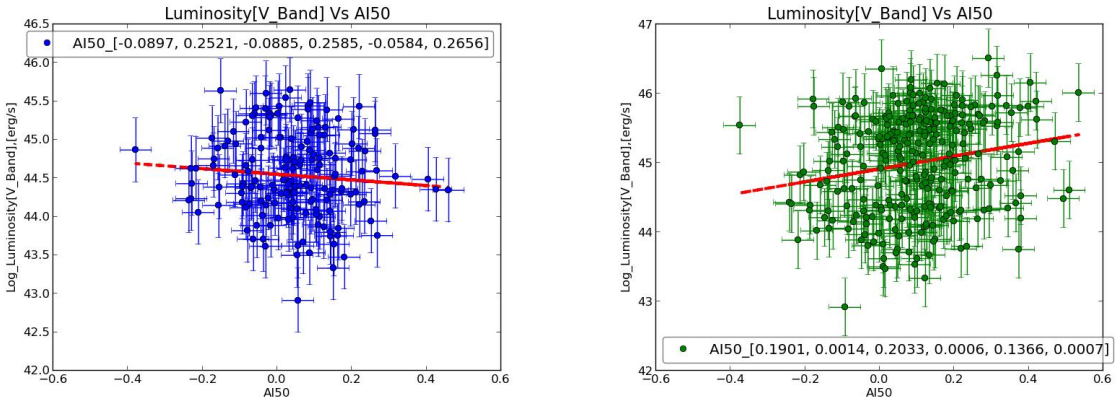


Figure 39: Relation of the AI50 of $H\alpha$ and $H\beta$ emission line profiles with V Band Luminosity

Table 7: Correlation Coefficients for V-Band Luminosity Verses $H\beta$ Asymmetry

Percentile	ρ_p	$P_p-value$	ρ_s	$P_s-value$	ρ_k	$P_k-value$	m	b
20	0.3415	0.0000	0.3679	0.0000	0.2536	0.0000	1.6778	44.6916
30	0.3075	0.0000	0.3288	0.0000	0.2283	0.0000	1.5719	44.7758
40	0.2292	0.0001	0.2489	0.0000	0.1686	0.0000	1.1768	44.8697
50	0.1901	0.0014	0.2033	0.0006	0.1366	0.0007	0.9263	44.9124
60	0.1589	0.0078	0.1695	0.0045	0.1130	0.0049	0.7429	44.9354
70	0.1313	0.0283	0.1360	0.0231	0.0902	0.0247	0.5489	44.9612

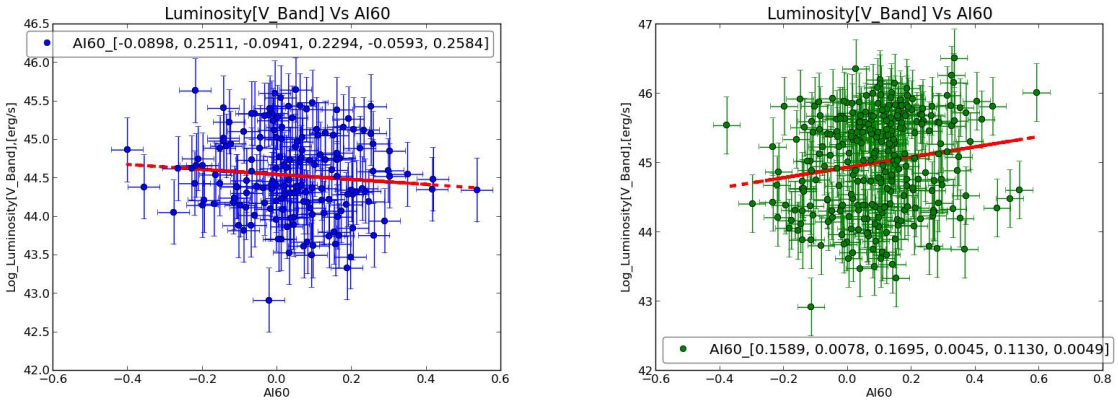


Figure 40: Relation of the AI60 of $H\alpha$ and $H\beta$ emission line profiles with V Band Luminosity

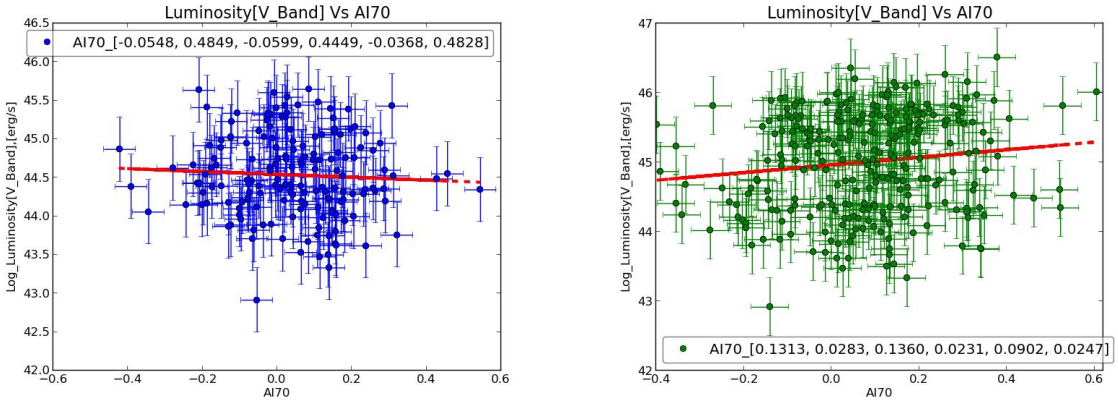


Figure 41: Relation of the AI70 of $H\alpha$ and $H\beta$ emission line profiles with V Band Luminosity

dius and increasing BH mass. This seems to point to a asymmetry arising from any of the factors that positively correlate with luminosity. This means a tendency of highly luminous sources giving rise to asymmetric $H\beta$ profiles. The gradient in the relation is observed to fall as one moves from the low percentiles to the high ones, a 10% percentile having a ~ 1.7 gradient and an 80% percentile having a gradient of ~ 0.3.

3.4.3 Relation of Asymmetry Index to the Radio Flux (Core-Radio Flux)

One of the kinds of AGN are in radio galaxies (Urry & Padovani 1995; Peterson 1997). A bulk of the emission from such sources lies in the radio regime. A number of authors (Pearson & Readhead 1988; McCarthy et al. 1991) have studied the behavior of galaxies with radio emission and all have observed asymmetry in many emission lines from radio galaxies (De Breuck et al. 2000). Even a study on the behavior of jets in weak radio sources noted asymmetry in spectral lines observed (Laing et al. 1999). It is this strong foundation that encourages us to systematically study the relation of radio Flux to the asymmetry of the emission lines. Our study is important since the spectral line asymmetry is binned in percentiles, making it easy to notice while part of the emission line responds more to the radio emission. In this study, the core radio flux at 6.0 arc secs is obtained. This is because radio flux can be extended to several tens of arc secs yet our interest is the radio flux emanating or very close to the BLR, in which the broad Balmer lines are formed.

The following plots are paired for each percentile, having a relation with the $H\alpha$ emission line on the left and that of the $H\beta$ emission line on the right. We analyze each percentile separately starting with the lowest percentile, the FWZI, to the highest part of te emission line possible, $90\&$ of the broad Balmer line.

Figure 42 is displaying the correlation between radio flux and asymmetry at 20% of the line profiles. The same behavior of $H\beta$ profile asymmetry being positively correlated with radio flux. However too in this case, the $H\alpha$ profile asymmetry correlation is flat.

Figures 43, 44, 45, 46 and 47 all show the pattern of the most asymmetric $H\alpha$ and $H\beta$ profiles positively correlating with core radio flux.

From the relations of asymmetry with radio flux, it has been noted that binning the profile is important in finding out which section of the profile responds more to the radio emission. The top part of the profile does not respond to changes in radio emission as the centroid of the profile. It is also noted that the $H\alpha$ and $H\beta$ profile shape is consistent with its response to radio flux throughout all the percentiles, although it the relation is weaker in the $H\alpha$ asymmetry.

3.4.4 Relation of Asymmetry Index to the Ionization degree

The Ionization degree is a measure of the excitation degree of the region from where the lines used to measure the ratio arise from. It is vital for us, since it will give us a clue to how asymmetric profiles relate to this ionization potential of the regions. A direct relation will give more insight to a wind scenario from the broad line region to the narrow line region in which these emission lines are obtained.

In the plots to follow, we have analyzed two measures of excitation, [OIII]/[OI] in red, and [OIII]/[OII] in blue. We go ahead to analyze the relations separately for each percentile. As in previous plots, $H\alpha$ profile analysis is on the left and $H\beta$ profile analysis on the right of each figure.

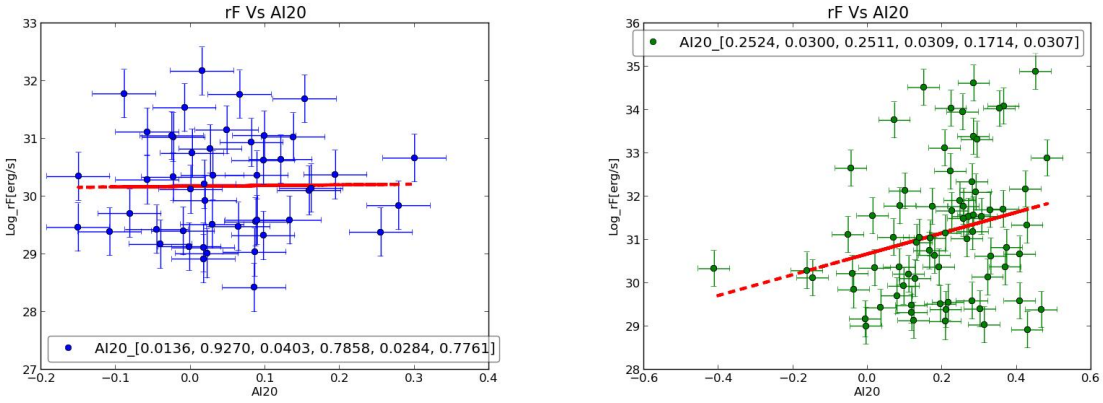


Figure 42: Relation of the AI20 of $H\alpha$ and $H\beta$ emission line profiles with Core Radio Flux

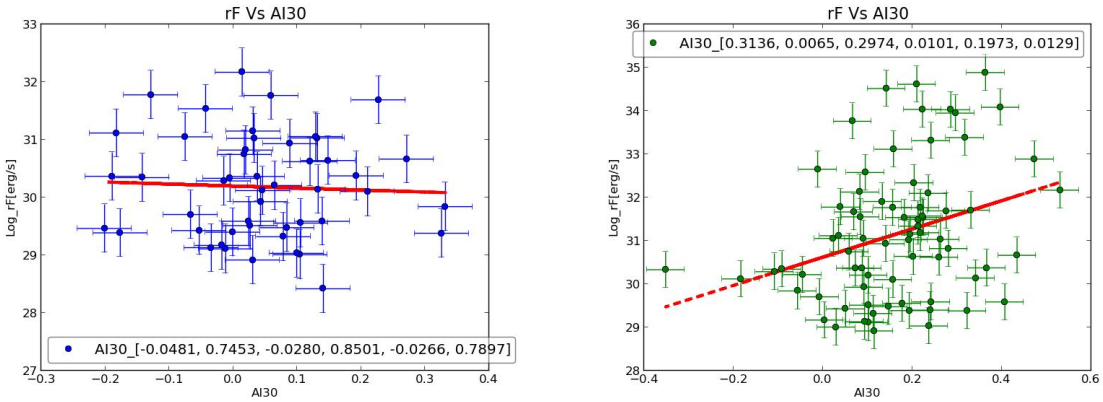


Figure 43: Relation of the AI30 of $H\alpha$ and $H\beta$ emission line profiles with Core Radio Flux

Table 8: Correlation Coefficients for $H\alpha$ relations

Percentile	ρ_p	$P_p-value$	ρ_s	$P_s-value$	ρ_k	$P_k-value$	m	b
20	0.0136	0.9270	0.0403	0.7858	0.0284	0.7761	0.1207	22.2540
30	-0.0481	0.7453	-0.0280	0.8501	-0.0266	0.7897	-0.3450	22.2752
40	-0.0698	0.6371	-0.0455	0.7589	-0.0355	0.7222	-0.4732	22.2829
50	0.0157	0.9156	0.0688	0.6421	0.0496	0.6187	0.0988	22.2544
60	0.1455	0.3238	0.1424	0.3342	0.0798	0.4238	0.8695	22.2000
70	0.2359	0.1065	0.2085	0.1549	0.1259	0.2069	1.2763	22.1829

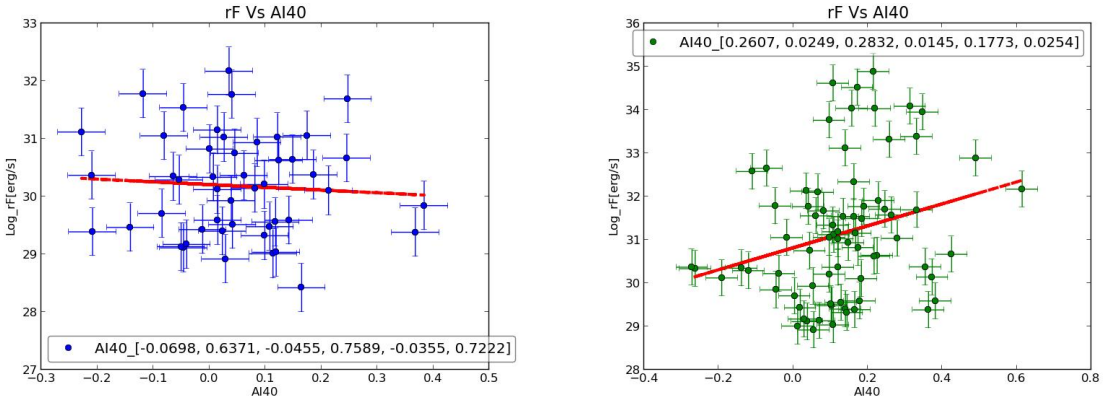


Figure 44: Relation of the AI40 of $H\alpha$ and $H\beta$ emission line profiles with Core Radio Flux

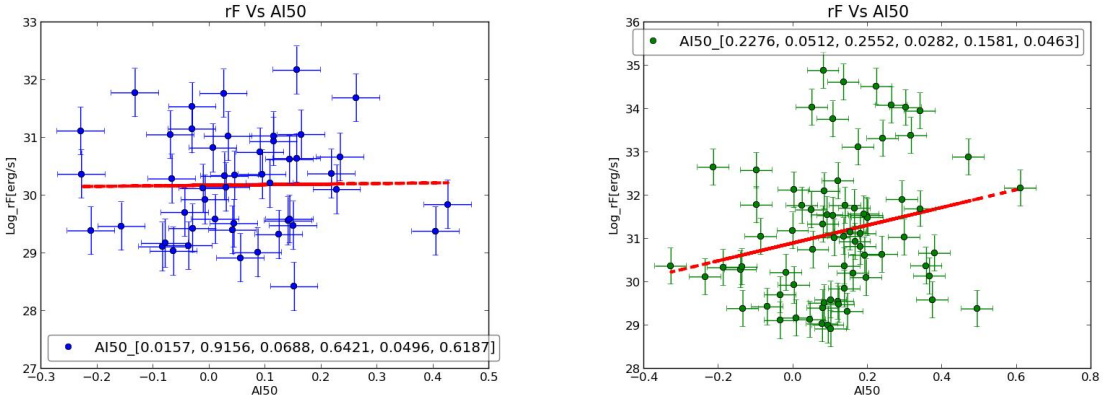


Figure 45: Relation of the AI50 of $H\alpha$ and $H\beta$ emission line profiles with Core Radio Flux

Table 9: Correlation Coefficients for $H\beta$ relations

Percentile	ρ_p	$P_p-value$	ρ_s	$P_s-value$	ρ_k	$P_k-value$	m	b
20	0.2524	0.0300	0.2511	0.0309	0.1714	0.0307	2.4011	22.7527
30	0.3136	0.0065	0.2974	0.0101	0.1973	0.0129	3.2619	22.6989
40	0.2607	0.0249	0.2832	0.0145	0.1773	0.0254	2.5361	21.6919
50	0.2276	0.0512	0.2552	0.0282	0.1581	0.0463	2.0519	22.9814
60	0.2494	0.0321	0.2372	0.0418	0.1448	0.0680	2.3258	22.9817
70	0.2288	0.0499	0.2476	0.0335	0.1670	0.0353	1.9114	23.0574

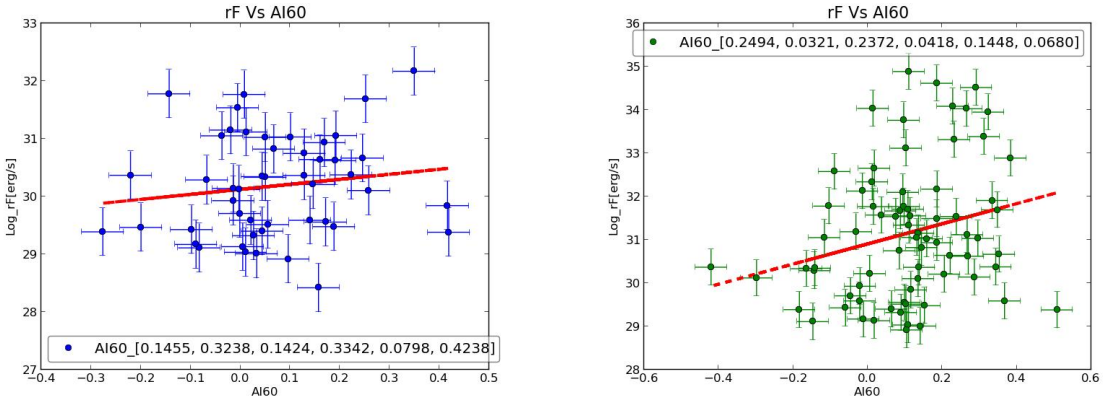


Figure 46: Relation of the AI60 of $H\alpha$ and $H\beta$ emission line profiles with Core Radio Flux

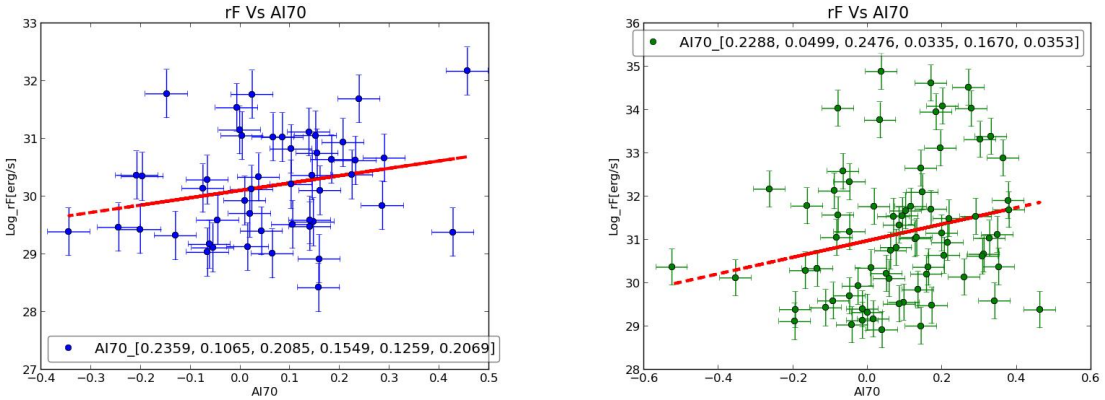


Figure 47: Relation of the AI70 of $H\alpha$ and $H\beta$ emission line profiles with Core Radio Flux

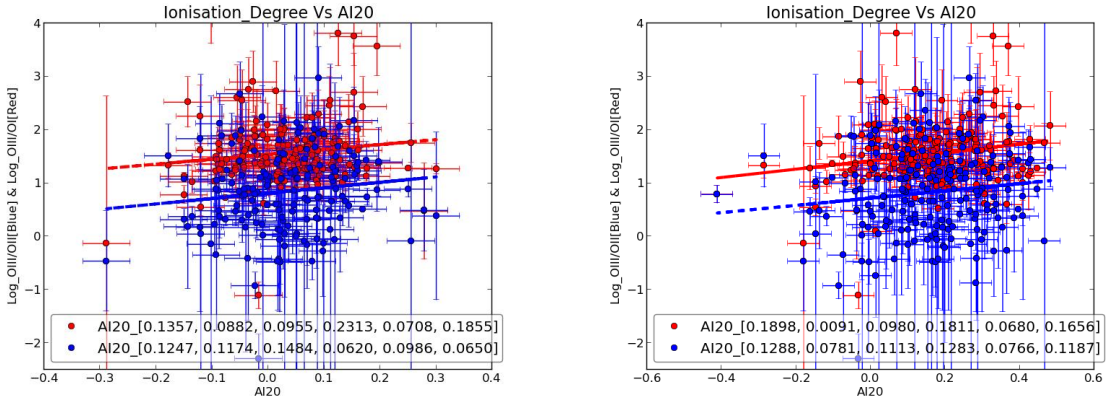


Figure 48: Relation of the AI20 of $H\alpha$ and $H\beta$ emission line profiles with Ionization Degree

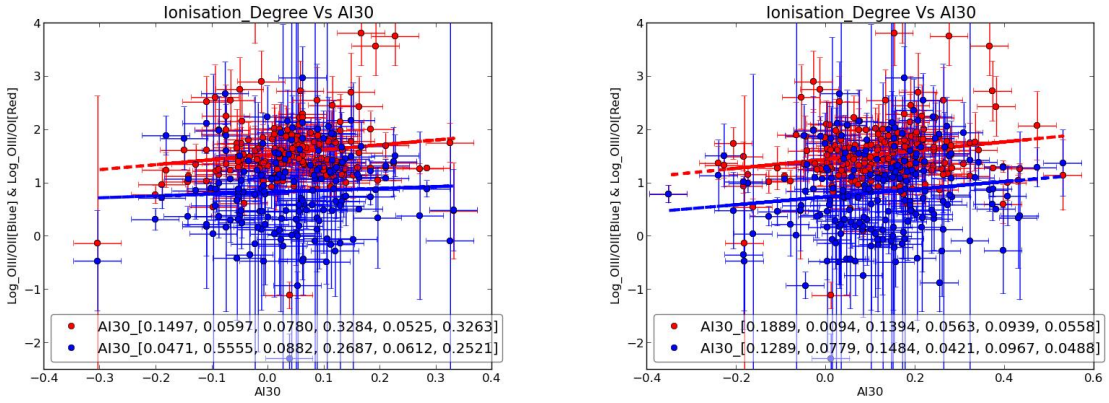


Figure 49: Relation of the AI30 of $H\alpha$ and $H\beta$ emission line profiles with Ionization Degree

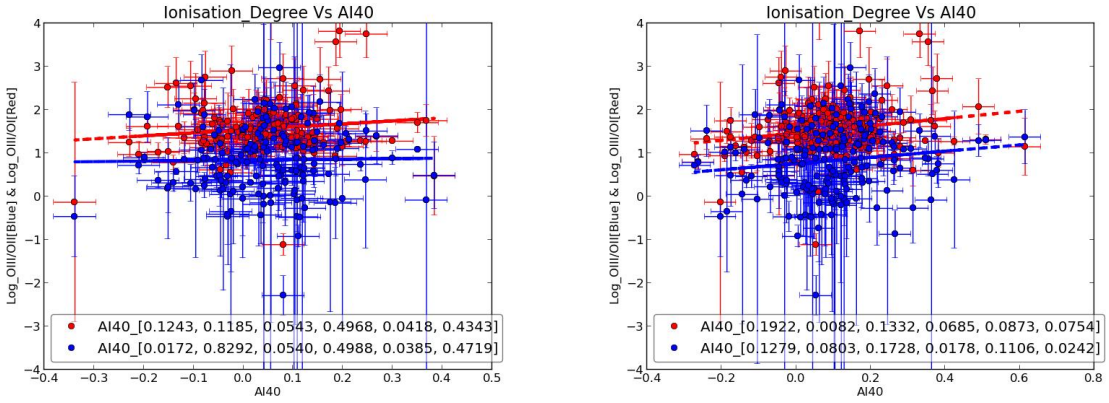


Figure 50: Relation of the AI40 of $H\alpha$ and $H\beta$ emission line profiles with Ionization Degree

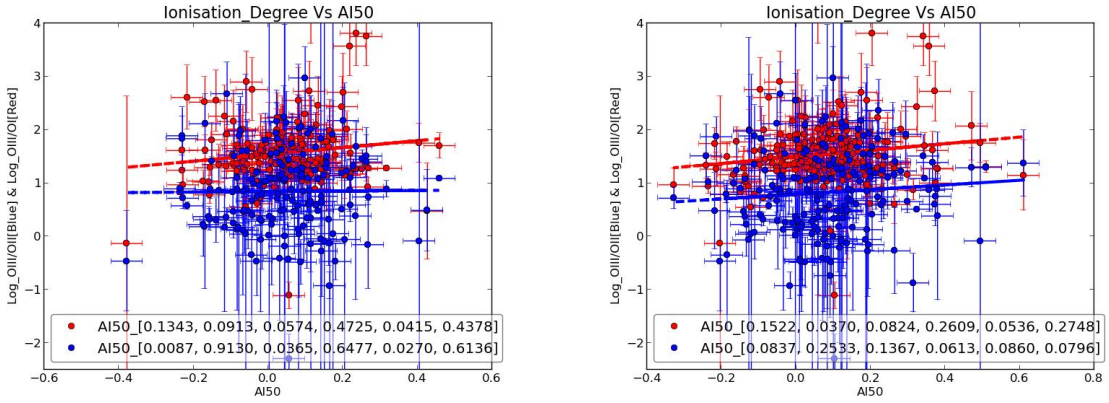


Figure 51: Relation of the AI50 of $H\alpha$ and $H\beta$ emission line profiles with Ionization Degree

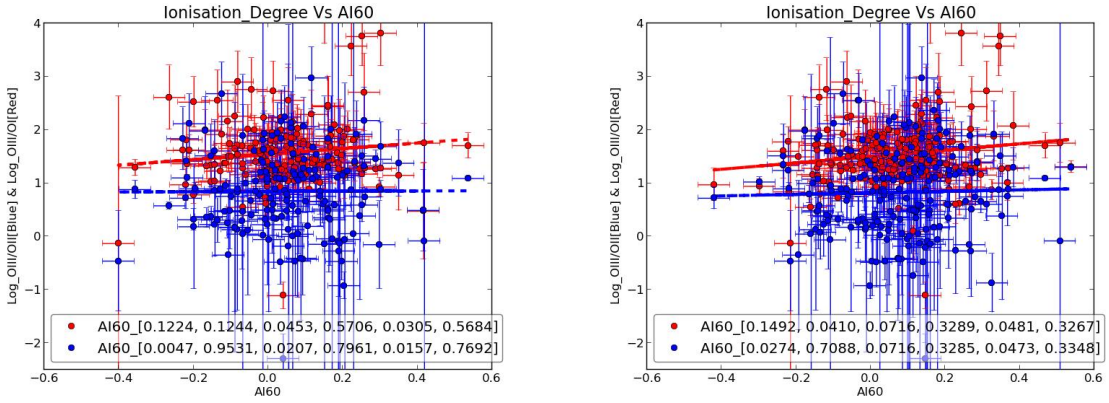


Figure 52: Relation of the AI60 of $H\alpha$ and $H\beta$ emission line profiles with Ionization Degree

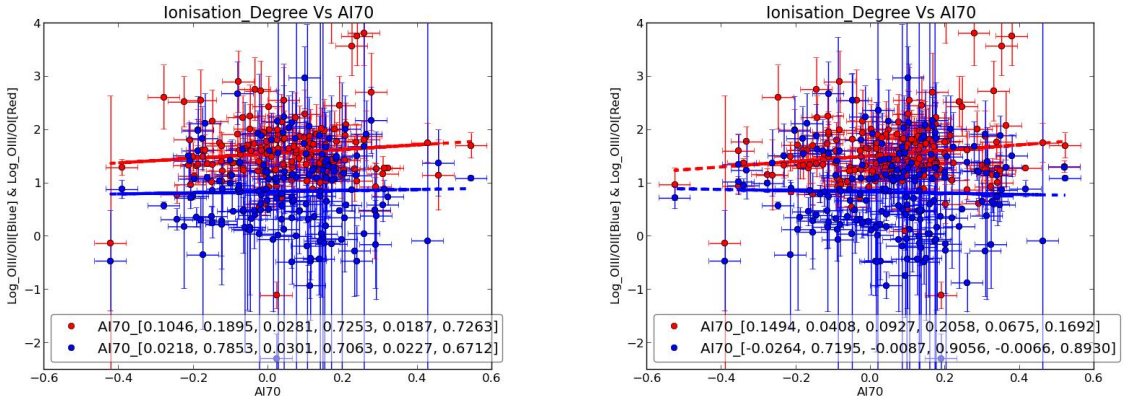


Figure 53: Relation of the AI70 of $H\alpha$ and $H\beta$ emission line profiles with Ionization Degree

For all the relations of ionization degree with asymmetry, it is maintained from figure 48 all through to 53 that it is very difficult to obtain a precise correlation of ionization degree with Balmer line asymmetry.

Statistical analyses show that the $H\beta$ relations are more reliable than $H\alpha$ measurements as seen from the $P - values$ and correlation coefficients.

3.5 Kurtosis Index relation to other kinematic properties

The way a profile changes, or how steep it may be, the Kurtosis Index, is a useful tool to use in studying other kinematic properties of the source because its a visual property. Once one knows how this measure is related to other indirect kinematic properties, it becomes easier to infer such properties by a simple analysis of the profile shape.

3.5.1 Relation of Kurtosis Index with Line Width (FWHM)

Since the Line width is a measure of the strength of the spectral features in the emission line, relating the Kurtosis with line width is simply relating the strength of the spectral features to the steepness (shape) of a profile.

Fig 54 shows how the Kurtosis varies with both Balmer emission lines. The $H\beta$ providing a tighter correlation than the $H\alpha$. But still one thing in evident, higher values of Kurtosis, translate to higher line widths generally. This suggests that broader profiles are flatter as previous studies show (Basu (1994)). Basu (1994) found a good correlation between FWHM and kurtosis, in which he noted that Balmer lines and other permitted lines are broader and flatter. This means that very broad lines experience less change in their shape parameters than less broadened lines. As seen in tables 14 and 15, the correlations are reliable with the $H\beta$ profile kurtosis index being tighter and steeper.

3.5.2 Relation of Kurtosis Index with Luminosity (V Band)

The relation of Kurtosis with Luminosity is also clearer with the $H\beta$ profile kurtosis. $H\alpha$ profile kurtosis relation is flat . This trend suggests that the most luminous sources will most likely have $H\beta$ profiles with extended wings. Although they both show Kurtosis Index decreasing with increasing Luminosity, the $P-values$ of the correlations are too high for us to rely on this trend only. However, this points to the direction that luminosity most likely is one tool to look at when studying accretion disk winds.

3.5.3 Relation of Kurtosis Index with Radio Flux (Core-Radio Flux)

$H\alpha$ kurtosis displays a positive correlation while $H\beta$ kurtosis shows an almost flat correlation. These relations of radio flux to kurtosis make is challenging to extract a meaningful trend of radio flux with profile kurtosis. Previous studies by Whittle (1985a) showed a that radio flux varied for different kinds of AGN. In our data, we did not separate the kind of AGN, thus making it impossible to see any relation. He found out that there was a significant difference between the profile kurtosis of linear sources and non-linear sources, with linear sources having steeper sided profiles. He went ahead to say that such observations could be naturally explained if the NLR gas at each end of the jet were radiating with opposite Doppler shifts relative to the synthetic(line-center) velocity. This means that the jets associated with the linear sources would perturb the outer parts of the velocity field, broadening the core to produce a high-kurtosis value, although the perturbation

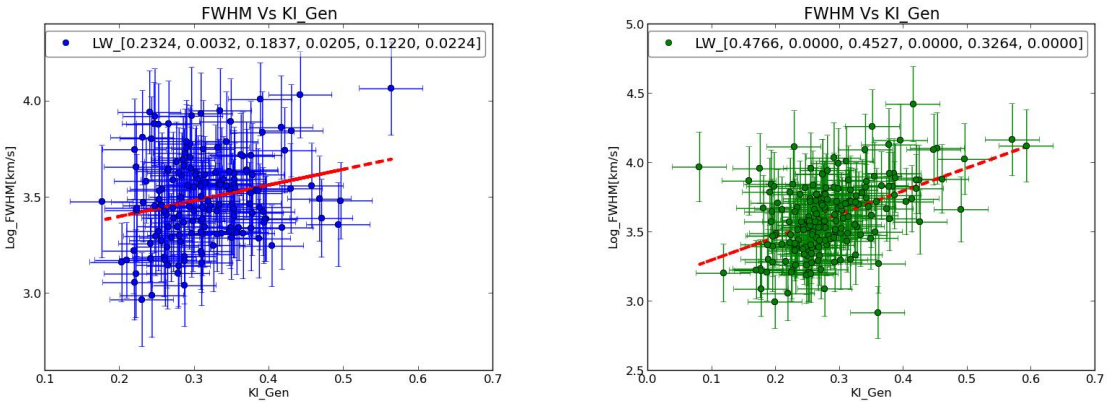


Figure 54: Relation of the Line Width of $H\alpha$ and $H\beta$ emission line profiles with Kurtosis Index

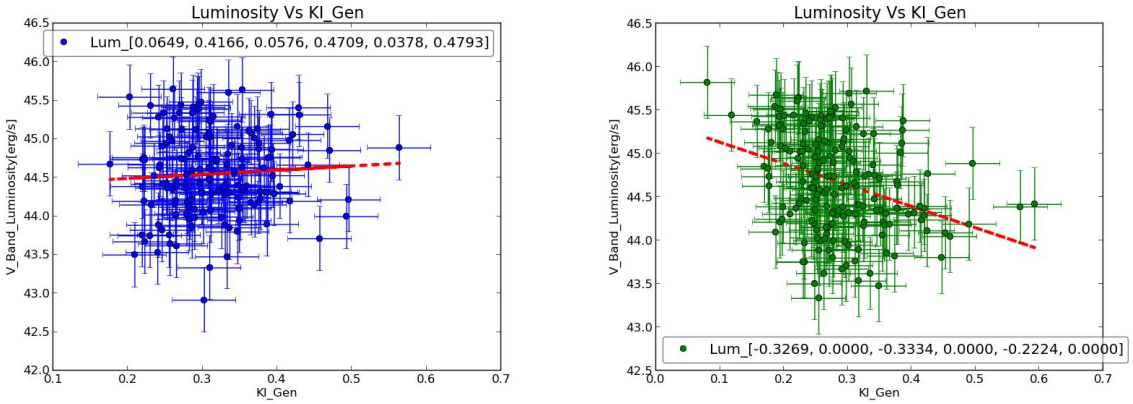


Figure 55: Relation of the V Band Luminosity of with Kurtosis Index

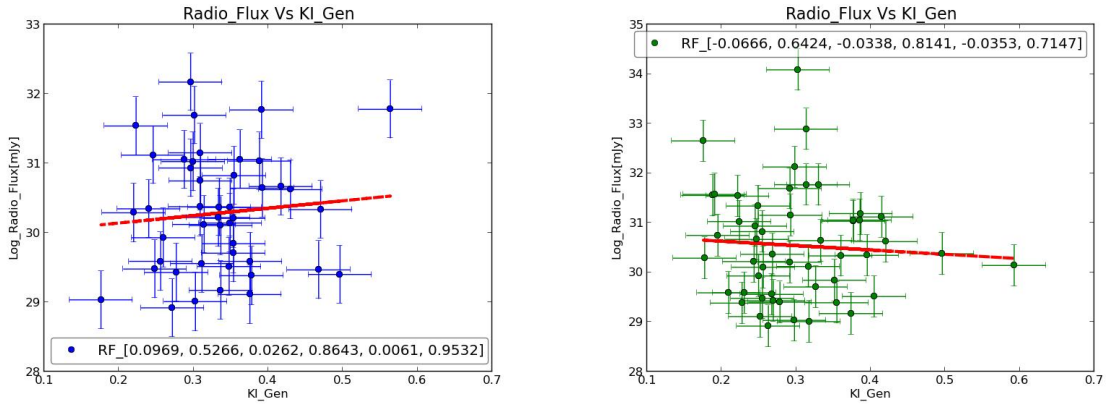


Figure 56: Relation of the core Radio Flux with Kurtosis Index

is not strong enough to influence the profile asymmetry.

3.5.4 Relation of Kurtosis Index with Ionization degree

The ionization degree here will be related to the excitation state of the NLR. The correlations between profile shape and the NLR excitation state are potentially very important because they reveal the presence of dynamical interactions between moving BLR moving gas(winds) and their environment. We have looked at two parameters of excitation degree, [OIII]/[OI] in red, and [OIII]/[OII] in blue. These values were obtained from the spectra of the data downloaded from SDSS. In general, the dispersion in excitation degree reduces with flatter profiles as observed in both $H\alpha$, on the left, and in $H\beta$ to the right of figure 57. Since the flatter profiles are generally the more asymmetric ones, then there is a view that more asymmetric profiles have less excitation degrees. Whittle (1985b) found out that there was a correlation between dust and asymmetry, where it was noted that an increase in extinction matched higher asymmetric profiles. High asymmetry correlates with low values of kurtosis. This meant that dust not only causes profile asymmetry but also softens the ionizing radiation field which consequently produces lower excitation NLR. Thus in the presence of dust, it is not easy to obtain a direct correlation between Kurtosis and the BLR winds or moving clouds.

4 Discussion

In the last section, we displayed the results obtained from the analysis of the Asymmetry Index and Kurtosis Index. We also looked at how the Asymmetry Index and Kurtosis Index relates to some other kinematic properties such as line width, luminosity,radio flux and ionization degree. It this chapter we shall discuss some of the most striking relations that were observed and, if possible, study the most likely implications of the relation to understanding the structure and properties of the accretion disk winds in AGN.

4.1 Asymmetry Index

Astrophysical line profiles are observed to display a variety of shapes. This is because

Table 10: Correlation Coefficients for $\frac{[OIII]}{[OI]}$ Ionization Degree Verses $H\alpha$ Asymmetry

Percentile	ρ_p	$P_p-value$	ρ_s	$P_s-value$	ρ_k	$P_k-value$	m	b
20	0.1357	0.0882	0.0955	0.2313	0.0708	0.1855	0.9175	1.5411
30	0.1497	0.0597	0.0780	0.3284	0.0525	0.3263	0.9266	1.5335
40	0.1243	0.1185	0.0543	0.4968	0.0418	0.4343	0.6905	1.5390
50	0.1343	0.0913	0.0574	0.4725	0.0415	0.4378	0.6414	1.5407
60	0.1224	0.1244	0.0453	0.5706	0.0305	0.5684	0.5182	1.5459
70	0.1046	0.1895	0.0281	0.7253	0.0187	0.7263	0.4225	1.5504

Table 11: Correlation Coefficients for $\frac{[OIII]}{[OII]}$ Ionization Degree Verses $H\alpha$ Asymmetry

Percentile	ρ_p	$P_p-value$	ρ_s	$P_s-value$	ρ_k	$P_k-value$	m	b
20	0.1247	0.1174	0.1484	0.0620	0.0986	0.0650	1.0134	0.8136
30	0.0471	0.5555	0.0882	0.2687	0.0612	0.2521	0.3505	0.8314
40	0.0172	0.8292	0.0540	0.4988	0.0385	0.4719	0.1151	0.8399
50	0.0087	0.9130	0.0365	0.6477	0.0270	0.6136	0.0501	0.8428
60	0.0047	0.9531	0.0207	0.7961	0.0157	0.7692	0.0239	0.8439
70	0.0218	0.7853	0.0301	0.7063	0.0227	0.6712	0.1057	0.8402

Table 12: Correlation Coefficients for $\frac{[OIII]}{[OI]}$ Ionization Degree Verses $H\beta$ Asymmetry

Percentile	ρ_p	$P_p-value$	ρ_s	$P_s-value$	ρ_k	$P_k-value$	m	b
20	0.1898	0.0091	0.0980	0.1811	0.0680	0.1656	0.7812	1.4197
30	0.1889	0.0094	0.1394	0.0563	0.0939	0.0558	0.8271	1.4452
40	0.1922	0.0082	0.1332	0.0685	0.0873	0.0754	0.8391	1.4654
50	0.1522	0.0370	0.0824	0.2609	0.0536	0.2748	0.6199	1.4930
60	0.1492	0.0410	0.0716	0.3289	0.0481	0.3267	0.5974	1.4997
70	0.1494	0.0408	0.0927	0.2058	0.0675	0.1692	0.5168	1.5130

Table 13: Correlation Coefficients for $\frac{[OIII]}{[OII]}$ Ionization Degree Verses $H\beta$ Asymmetry

Percentile	ρ_p	$P_p-value$	ρ_s	$P_s-value$	ρ_k	$P_k-value$	m	b
20	0.1288	0.0781	0.1113	0.1283	0.0766	0.1187	0.6798	0.7197
30	0.1289	0.0779	0.1484	0.0421	0.0967	0.0488	0.7236	0.7414
40	0.1279	0.0803	0.1728	0.0178	0.1106	0.0242	0.7158	0.7608
50	0.0837	0.2533	0.1367	0.0613	0.0860	0.0796	0.4372	0.7920
60	0.0274	0.7088	0.0716	0.3285	0.0473	0.3348	0.1407	0.8178
70	-0.0264	0.7195	-0.0087	0.9056	-0.0066	0.8930	-0.1170	0.8355

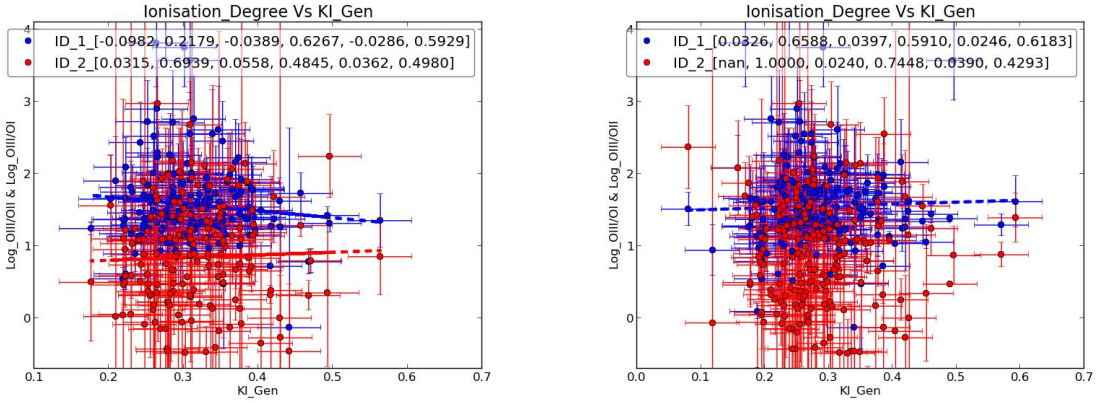


Figure 57: Relation of the Ionization Degree with Kurtosis Index

Table 14: Correlation Coefficients for the Kinematic Properties Verses $H\alpha$ Kurtosis Index

Relation	ρ_p	$P_p-value$	ρ_s	$P_s-value$	ρ_k	$P_k-value$	m	b
LW	0.2324	0.0032	0.1837	0.0205	0.1220	0.0224	0.8158	3.2392
RF	0.0969	0.5266	0.0262	0.8643	0.0061	0.9532	1.0674	29.9262
L	0.0649	0.4166	0.0576	0.4709	0.0378	0.4793	0.5398	44.3827
ID_1	-0.0982	0.2179	-0.0389	0.6267	-0.0286	0.5929	-0.9613	1.8726
ID_2	0.0315	0.6939	0.0558	0.4845	0.0362	0.4980	0.3699	0.7284

Table 15: Correlation Coefficients for the Kinematic Properties Verses $H\beta$ Kurtosis Index

Relation	ρ_p	$P_p-value$	ρ_s	$P_s-value$	ρ_k	$P_k-value$	m	b
LW	0.4766	0.0000	0.4527	0.0000	0.3264	0.0000	1.6614	3.1338
RF	-0.0666	0.6424	-0.0338	0.8141	-0.0353	0.7147	-0.8794	30.8045
L	-0.3269	0.0000	-0.3334	0.0000	-0.2224	0.0000	-2.4625	45.3767
ID_1	0.0326	0.6588	0.0397	0.5910	0.0246	0.6183	0.2657	1.4750
ID_2	nan	1.0000	0.0240	0.7448	0.0390	0.4293	nan	nan

the shape of a line profile can depend on a number of parameters which include; shocks, inflows and outflows of a wind component, obscuration by dust and rotation. If we only take the effect of the velocity field, that is shocks, Doppler motions, turbulence, inflow and outflow wind components and rotation, we can separate the region of the line profile that suffers from each effect. Since the line width is an excellent measure of strength of the properties of the line profile, we shall keep its relation to asymmetry in mind while discussing the rest of the kinematic properties.
We shall not include relations obtained at 00% percentiles since errors in that measurement were higher than for other parts of the profile due to the difficulty in estimating the continuum levels at both ends of the broad Balmer lines. (Balcells 1991) studied asymmetric line profiles in merger remnants, the study in his models suggesting that the asymmetry is not due to a disk of accreted secondary material; it is intrinsic to the distribution of primary particles, and has been added during the merger. It is argued that the asymmetries are a consequence of the transfer of the orbital energy and angular momentum to the primary particles during the merger; for the mergers studied in his models, profile asymmetries are a relic of the formation dynamics rather than the signature of superimposed components. Relating this to our case of the BLR, the asymmetries may be due to the transfer of the orbital energy and angular momentum of the accreting material and it is a relic of the material falling in or leaving the accretion disk. This material flows in or out in form of a wind. According to Gaskell & Goosemann (2013), a line shifts, thus asymmetry, in the base of a profile is a reflection of high accretion rates of the AGN. They demonstrated that high accretion rate AGNs will show line blue shifts, both in their models and observational data. For our case, most of the Balmer emission line asymmetries were red-shifted, indicating outflow of material (wind) rather than inflow (accretion).

4.1.1 Line Width

Line width are a good measure in investigating the strength of the spectral features in a system. Some authors use it to differentiate Seyfert galaxies from other emission line galaxies (Feldman et al. 1982). Others, use it to separate quasars in two populations, Population A and Population B in which the later have extremely broad Balmer emission lines exceeding a width of 3000 km/s. The line width of the emission line profiles might depend on the the velocity field, geometry of the line emiting gas, obscuring effects, the superposition of line emission from different regions and on isotropy/anisotropy of the

line emission (Kollatschny & Zetzl 2012). In the relations with asymmetry, it was observed that $H\alpha$ profiles showed a negative correlation, while the $H\beta$ profiles displayed a positive correlation. This would mean that the line width as a measure of the spectral features strength of the line emitting region will provide better results when we use the $H\beta$ line asymmetry relation to line width. High values in line width were observed to correlate with higher values in asymmetry for the $H\beta$ profiles. This may suggest that systems with high values in $H\beta$ profile asymmetry have within them lots of information that we can obtain on the velocity field and geometry of the line emitting gas, whereas those with less $H\beta$ asymmetry carried less information that can be extracted about the geometry of the line emitting gas.

In this case it is the $20\%, 30\%, 40\%, 50\%\ and\ 60\%\ H\beta$ emission line percentiles displaying good correlations to support this.

4.1.2 Luminosity

Luminosity is another property that is widely studied, having many relations (Padovani & Rafanelli 1988) with other properties of host galaxies (La Mura et al. 2009) like among other properties, the BLR size and BH mass. Although the scatter was high, some plots appeared to suggest that highly asymmetric profiles correlated with high luminosities. This means these luminosities are being driven by the same mechanism giving rise to asymmetry. This means winds will create asymmetry and also rise the luminosity of the source as seen in such relations. The best relations were obtained in $H\beta$ profile asymmetry for the $10\%, 20\%, 30\%,\ and\ 40\%$ percentiles. The moderately tight positive correlations point to a direction in which we notice that the most luminous sources have high asymmetries in their $H\beta$ emission line profiles.

4.1.3 Radio Flux

The radio flux scaled in such a way that high $H\beta$ emission line asymmetries positively correlated with radio flux. The clearest relations are in $20\%, 30\%, 40\%, 50\%\ and\ 60\%$ $H\beta$ emission line percentiles as seen in fig 60. (Corbin 1997), in his study of "The Emission-Line Properties of Low-Redshift Quasi-stellar Objects. II. The Relation to Radio Type", found out that FRS quasars have significantly wider and more red-ward asymmetric $H\beta$ profiles. Studies on the $H\alpha$ Balmer emission line in Solar Physics by (Ichimoto & Kurokawa 1984) noted red asymmetry of H-alpha flare line profiles. They believed that the Red-shifted emission streaks of H-alpha line are found at the initial phase of almost all flares which occur near the disk center, and are considered to be substantial features of the asymmetry. It is found that a downward motion in the flare chromospheric region is the cause of the red-shifted emission streak. The downward motion abruptly increases at the onset of a flare, attains its maximum velocity of about 40 to 100 km/s shortly before the impulsive peak of the microwave burst, and rapidly decreases before the intensity of H-alpha line reaches its maximum. This proves that high radio emission can cause asymmetry in emission line shapes and the asymmetry is a consequence of motion material that is giving rise to the emission line.

4.1.4 Ionization Degree

The ionization degree in the narrow line region has also been noted to respond with effects taking place in the broad line region. For an outflow,a wind from an accretion disk would drive gas and dust out of the broad line region (Kollatschny & Zetzl 2013).

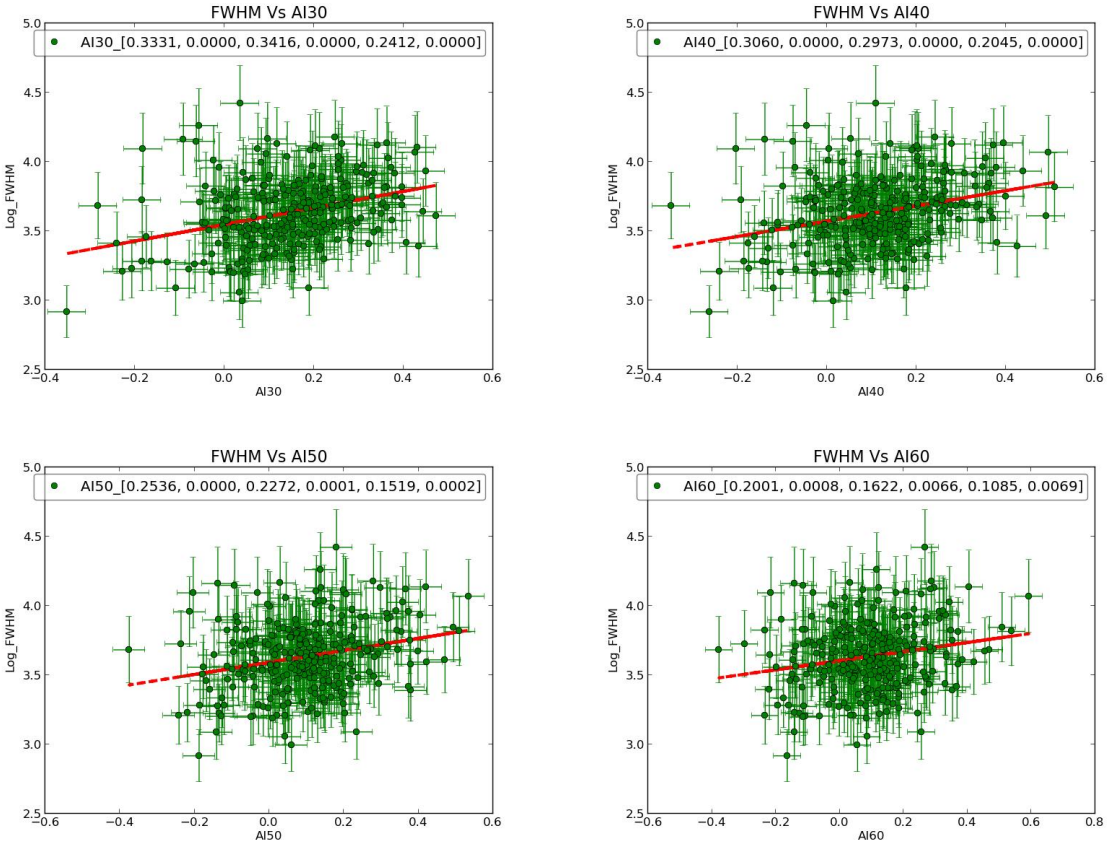


Figure 58: Relation of the AI00 of $H\alpha$ and AI10 $H\beta$ emission line profiles with Line width

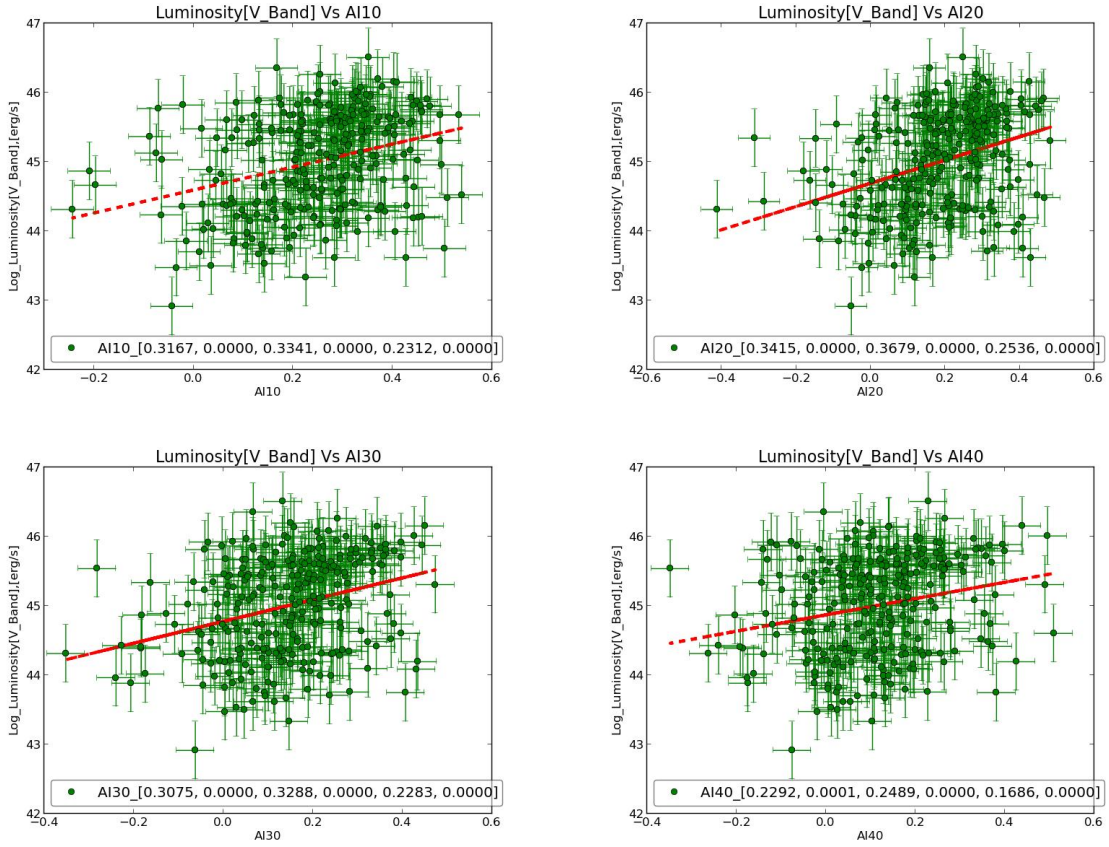


Figure 59: Relation of the AI00 of $H\alpha$ and AI10 $H\beta$ emission line profiles with Line width

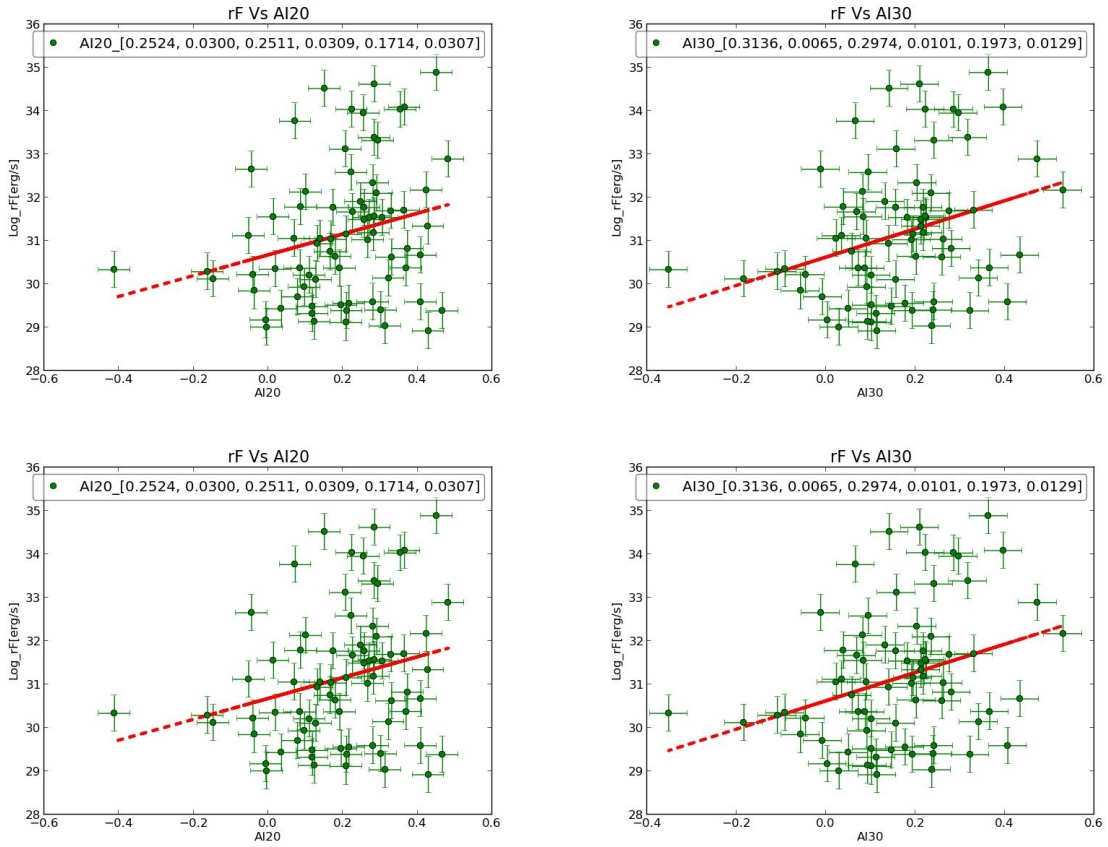


Figure 60: The Relation of the AI20 of $H\beta$ and AI30 of $H\beta$ emission line profiles with Core Radio Flux

This would cause both cooling and heating consequences in the narrow line region and this has been observed in the high variance in ionization degree for higher asymmetries. An inflow would also rid the narrow line region of material that would contribute to either heating or cooling, thus having still a dispersion in ionization degree measurements.

In all the properties studied, it seems plausible to confirm that accretion disk winds are part of the reason to the asymmetry in emission line profiles, both directly and indirectly. It is also noted that whether its inflow or outflow, the results would be similar although the most studied relations favor outflows.

The clear relations in this case can be seen in figure 61 which shows those of the 10th, 20th, 30th and 40th percentile from top left to right.

5 Conclusion

In this study we investigated the asymmetry in the first two broad Balmer emission lines, ($H\alpha$ & $H\beta$), with the aim of probing accretion disk winds in Active Galactic Nuclei (AGN). Our sample was chosen from the SDSS DR7 with slightly over 300 spectra. We extracted the individual broad Balmer emission lines from each spectrum, normalized them to have the emission line peak have a value of unity, and measured the line shifts at each chosen percentile after centering the profiles at the a wavelength value corresponding to the emission line peak. Line shift values were then used to calculate the Asymmetry Index (A.I) and Kurtosis Index (K.I) for each respective percentile, and statistical distribution of these measurements was analyzed, after which, both the AI and KI were plotted against some kinematic properties like line width (FWHM), Luminosity, Radio Flux, and Ionization degree ($\frac{[OIII]\lambda\ 5007}{[OI]\lambda\ 6302}$ & $\frac{[OIII]\lambda\ 5007}{[OII]\lambda\ 3727}$).

According to our results, we come to the following conclusions:

- Asymmetry in $H\beta$ profiles positively correlated with Line width, V-band Luminosity, Radio Flux and Ionization degree.

- Asymmetry in $H\beta$ profiles shows a stronger correlation with Line width, V-band Luminosity, Radio Flux and Ionization degree than that of $H\alpha$ emission line profiles. Its correlations were tighter, with steeper gradients.

- From the statistical distribution of the AI and KI, the asymmetry of the profiles is predominantly red-shifted.

- Broader lines showed more asymmetry than narrower ones.

- Overplots of $H\alpha$ profiles with $H\beta$ profiles from the same spectrum showed that the $H\beta$ profiles had an extended red asymmetry from their $H\alpha$ counterparts.

- The flux ratio $\frac{[OIII]\lambda\ 5007}{[OI]\lambda\ 6302}$, as a measure of ionization degree is more reliable than $\frac{[OIII]\lambda\ 5007}{[OII]\lambda\ 3727}$ since $[OII]\lambda\ 3727$ values contained more errors in their values.

- The observed distribution of the asymmetry is consistent with previous studies on many other emission and absorption lines, most showing positive asymmetries.

- Percentiles of $20\%, 30\%, 40\%, 50\%, 60\%$ and 80% contain the most reliable information about profile shape since they are least affected by errors due to continuum estimation and line peak estimation.

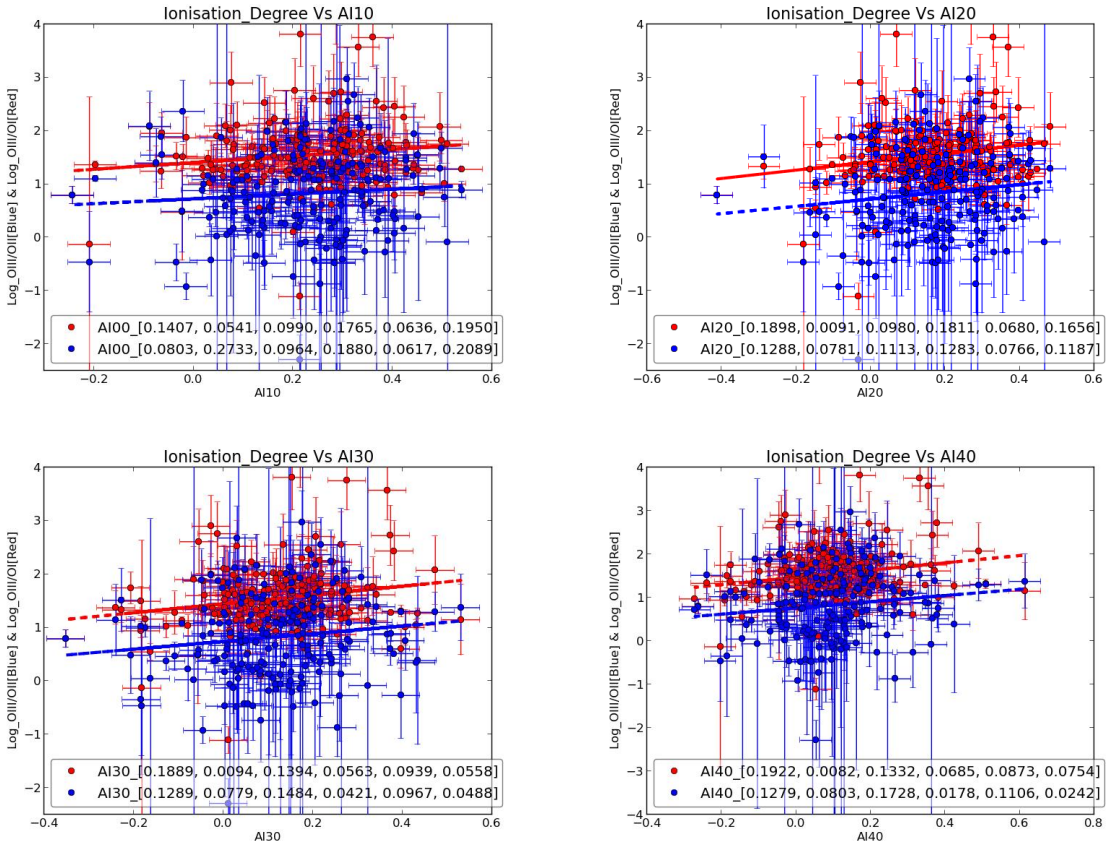


Figure 61: The Relation of the AI10, AI20, AI30, AI40 of $H\beta$ emission line profiles with Ionization Degree

- The line profile shape parameters carry much detailed information about kinematics of the BLR, which can be better understood by means of techniques exploiting the profile by region, rather than measuring general shape parameters.

Although this analysis may be an advancement in probing accretion disk winds, a study with more sources and incorporating many more other emission and absorption lines would be much better in drawing conclusive relations with the kinematic properties and thus key to understanding the structure of accretion disk winds in AGN.

References

Abazajian, K. N., Adelman-McCarthy, J. K., Agüeros, M. A., et al. 2009, The Astrophysical Journal, Supplement, 182, 543

Balcells, M. 1991, Astronomy and Astrophysics, 249, L9

Basu, D. 1994, Astrophysics and Space Science, 222, 91

BBC. 2013, Exploration of the Universe

Beazley, D. 2006, Python Essential Reference, Developer's library (Sams)

Blandford, R. D. & Znajek, R. L. 1977, Monthly Notices of the Royal Astromical Society, 179, 433

Bowman, K. P. 2005, An Introduction to Programming with IDL: Interactive Data Language (Academic Press)

Bregman, J. N. 1990, Astronomy and Astrophysics Review, 2, 125

Brotherton, M. S. 1996, The Astrophysical Journal, Supplement, 102, 1

Clavel, J., Boksenberg, A., Bromage, G. E., et al. 1990, Monthly Notices of the Royal Astronomical Society, 246, 668

Corbin, M. R. 1997, The Astrophysical Journal, Supplement, 113, 245

Dawson, M. 2003, Python Programming for the Absolute Beginner, For the absolute beginner (Premier Press)

De Breuck, C., Röttgering, H., Miley, G., van Breugel, W., & Best, P. 2000, Astronomy and Astrophysics, 362, 519

De Robertis, M. M. & Shaw, R. A. 1990, The Astrophysical Journal, 348, 421

Fehily, C. 2002, Python, Visual quickstart guide (Peachpit Press)

Feldman, F. R., Weedman, D. W., Balzano, V. A., & Ramsey, L. W. 1982, The Astrophysical Journal, 256, 427

Frieman, J. A., Bassett, B., Becker, A., et al. 2008, The Astronomical Journal, 135, 338

Gaskell, C. M. & Goosemann, R. W. 2013, The Astrophysical Journal, 769

Hamann, F. 1998, The Astrophysical Journal, 500, 798

Hao, L., Strauss, M. A., Tremonti, C. A., et al. 2005, The Astrophysical Journal, 129, 1783

Ichimoto, K. & Kurokawa, H. 1984, Solar Physics, 93, 105

Kaspi, S., Brandt, W. M., George, I. M., et al. 2002, The Astrophysical Journal, 574, 643

Kollatschny, W. & Zetzl, M. 2012, Astronomy and Astrophysics, 549, A100

Kollatschny, W. & Zetzl, M. 2013, Astronomy and Astrophysics, 551, L6

La Mura, G., Di Mille, F., Ciroi, S., Popović, L. Č., & Rafanelli, P. 2009, The Astrophysical Journal, 693, 1437

Laing, R. A., Parma, P., de Ruiter, H. R., & Fanti, R. 1999, Monthly Notices of the Royal Astronomical Society, 306, 513

Mark, S. 2009, Programming in Python 3 (Pearson Education)

McCarthy, P. J., van Breugel, W., & Kapahi, V. K. 1991, The Astrophysical Journal, 371, 478

Mehdipour, M., Branduardi-Raymont, G., Kaastra, J. S., et al. 2011, Astronomy and Astrophysics, 534, A39

Osterbrock, D. E. 1989, Astrophysics of gaseous nebulae and active galactic nuclei

Padovani, P. & Rafanelli, P. 1988, Astronomy and Astrophysics, 205, 53

Pearson, T. J. & Readhead, A. C. S. 1988, The Astrophysical Journal, 328, 114

Peterson, B. M. 1997, An Introduction to Active Galactic Nuclei

Peterson, B. M., Ferrarese, L., Gilbert, K. M., et al. 2004, The Astrophysical Journal, 613, 682

Russell, J. & Cohn, R. 2012, Qtiplot (Book on Demand)

SDSS. 2013, Sloan Digital Sky Survey, Data Release 7 –SDSSDR7

Thorne, A., Litzen, U., & Johansson, S. 1999, Spectrophysics

Tody, D. 1986, in Society of Photo-Optical Instrumentation Engineers (SPIE) Conference Series, Vol. 627, Society of Photo-Optical Instrumentation Engineers (SPIE) Conference Series, ed. D. L. Crawford, 733

Turner, T. J. & Pounds, K. A. 1989, Monthly Notices of the Royal Astronomical Society, 240, 833

Ulrich, M.-H., Maraschi, L., & Urry, C. M. 1997, Annual Reviews of Astronomy and astrophysics, 35, 445

Urry, C. M. & Padovani, P. 1995, Publications of the Astronomical Society of the Pacific, 107, 803

Valdes, F. 1986, in Society of Photo-Optical Instrumentation Engineers (SPIE) Conference Series, Vol. 627, Society of Photo-Optical Instrumentation Engineers (SPIE) Conference Series, ed. D. L. Crawford, 749–756

Whittle, M. 1985a, Monthly Notices of the Royal Astronomical Society, 213, 1

Whittle, M. 1985b, Monthly Notices of the Royal Astronomical Society, 213, 33

Yann, B., Rockosi, C., Newberg, H. J., et al. 2009, The Astronomical Journal, 137, 0004

York, D. G., Adelman, J., Anderson, Jr., J. E., et al. 2000, The Astronomical Journal, 120, 1579

Yu, X.-X. & Gan, W.-Q. 2006, Chinese Astronomy and Astrophysics, 30, 294